ESC-TR-96-060

Quarterly Technical Report

Solid State Research

1996:1

Lincoln Laboratory

MASSACHUSETTS INSTITUTE OF TECHNOLOGY

LEXINGTON, MASSACHUSETTS

Prepared for the Department of the Air Force under Contract F19628-95-C-0002.

Approved for public release; distribution is unlimited.

19970411 013

DTIC QUALITY INSPECTED 1

This report is based on studies performed at Lincoln Laboratory, a center for research operated by Massachusetts Institute of Technology. The work was sponsored by the Department of the Air Force under Contract F19628-95-C-0002.

This report may be reproduced to satisfy needs of U.S. Government agencies.

The ESC Public Affairs Office has reviewed this report, and it is releasable to the National Technical Information Service, where it will be available to the general public, including foreign nationals.

This technical report has been reviewed and is approved for publication.

FOR THE COMMANDER

Gary Tatungian
Administrative Contracting Officer
Contracted Support Management

Non-Lincoln Recipients

PLEASE DO NOT RETURN

Permission is given to destroy this document when it is no longer needed.

MASSACHUSETTS INSTITUTE OF TECHNOLOGY
LINCOLN LABORATORY

SOLID STATE RESEARCH

QUARTERLY TECHNICAL REPORT

1 NOVEMBER 1995–31 JANUARY 1996

ISSUED 25 SEPTEMBER 1996

LEXINGTON MASSACHUSETTS

DTIC QUALITY INSPECTED 1

IN APPRECIATION

For 29 years, as the head of the Solid State Division, Professor Alan L. McWhorter oversaw the publication of Lincoln Laboratory's Solid State Research reports. He upheld the scientific and editorial standards that made them valuable contributions to the literature in solid state materials, devices, and circuits.

Professor McWhorter's 43-year affiliation with Lincoln Laboratory began in 1953. As a graduate student at MIT, he was a research assistant in the Laboratory until 1955, when he became a full staff member. In 1959, he joined the faculty of the Department of Electrical Engineering and Computer Science at MIT, while maintaining his Laboratory affiliation as a technical consultant. In 1962, still on the faculty at MIT, he was appointed assistant head of the Solid State Division. Professor McWhorter was subsequently named associate head in 1963, and then division head in 1965, a position he held until 1994, when he became the Laboratory's first Fellow.

On his retirement in 1996, following a distinguished career at Lincoln Laboratory and MIT, Professor McWhorter's high goals and integrity in guiding the Laboratory's solid state research are acknowledged with deep respect and appreciation.

ABSTRACT

This report covers in detail the research work of the Solid State Division at Lincoln Laboratory for the period 1 November 1995 through 31 January 1996. The topics covered are Quantum Electronics, Electrooptical Materials and Devices, Submicrometer Technology, High Speed Electronics, Microelectronics, Analog Device Technology, and Advanced Silicon Technology. Funding is provided primarily by the Air Force, with additional support provided by the Army, ARPA, Navy, BMDO, NASA, and NIST.

TABLE OF CONTENTS

	In Appreciation	iii
	Abstract	v
	List of Illustrations	ix
	List of Tables	xiii
	Introduction	xv
	Reports on Solid State Research	xvii
	Organization	xxvii
1.	QUANTUM ELECTRONICS	1
1.1	Nd:YAG Sum-Frequency Source of Sodium-Resonance Radiation	1
2.	ELECTROOPTICAL MATERIALS AND DEVICES	9
2.1	Light Scattering in High-Dislocation-Density GaN	9
2.2	Optically Pumped GaN-AlGaN Double-Heterostructure Lasers Grown by ECR-MBE and HVPE	11
2.3	175-K CW Operation of InAsSb/InAlAsSb/InAs Quantum-Well Diode Lasers Emitting at 3.5 μm	17
3.	SUBMICROMETER TECHNOLOGY	23
3.1	High-Resolution Studies of Crystalline Damage Induced by Single-Point Diamond Machining of Silicon	23
4.	HIGH SPEED ELECTRONICS	31
4.1	Correlation of Optical Pulses with a Low-Temperature-Grown GaAs Photoconductor	31
5.	MICROELECTRONICS	35
5.1	Use of a Charge-Coupled Device as a Charged-Particle Spectrometer	35
6.	ANALOG DEVICE TECHNOLOGY	39
6.1	Microwave Power Dependence of $YBa_2Cu_3O_7$ Thin-Film Josephson Edge Junctions	39
7.	ADVANCED SILICON TECHNOLOGY	45
7.1	Laser-Programmable Gate Array	45

LIST OF ILLUSTRATIONS

Figure No.		Page
1-1	Schematic of laser system. The abbreviations shown in the figure are as follows: HR, high reflector; ZZS, zigzag slab; E, etalon; NLC, nonlinear crystal; ML, mode locker; OC, output coupler; VCL, vertical cylindrical lens; HCL, horizontal cylindrical lens; AL, adjustable spherical lens; SL, spherical lens; DM, dichroic mirror. The dual-crystal sum-frequency mixing apparatus is shown in Figure 1-3.	1
1-2	Schematic of diode-pumped, Nd:YAG, zigzag laser head. The path of the laser radiation inside the slab is shown to traverse a five-diamond path. The input surface is antireflection coated at the laser wavelength. The end surface is high-reflection coated at the laser wavelength, and for the 1319-nm laser this end is high-transmission coated for 1064-nm radiation. The Nd:YAG slab is 5.5 cm long, 2.5 cm thick, and 3.5 cm wide.	2
1-3	Schematic of dual-crystal sum-frequency mixing apparatus. The dichroic mirror has high reflectivity at 589 nm for *s*-polarization light and high transmissivity at 1064 and 1319 nm for *p*-polarization light.	4
1-4	Temporal envelopes of (a) 1064-, (b) 1319-, and (c) 589-nm mode-locked pulse train after passing through frequency mixing apparatus. The profiles with and without sum-frequency generation (SFG) were obtained by adjusting the relative timing of the mode-locked pulses so that there either was or was not temporal overlap of the pulses in the nonlinear crystals. Note that the 1064-nm laser pulse has a longer duration than the 1319-nm pulse. The diode pump radiation has a duration of 200 μs with the end of the Nd:YAG laser radiation marking the end of the diode pump radiation.	5
1-5	Temporal profiles of the (a) 1064-, (b) 1319-, and (c) 589-nm mode-locked pulses after passing through frequency mixing apparatus. Profiles with and without SFG were obtained as described in Figure 1-4.	6
2-1	Model of lightwave scattering by dislocation, where thick lines indicate wavefronts and dots indicate atoms in the crystal lattice. The extra plane of atoms in the upper region results in a phase delay in that portion of the wavefront. The wavefront deformation then gives rise to scattering loss. Note that the figure is not drawn to scale; the wavelength λ should be much greater than the atomic spacing d. The path length difference δ is also greatly exaggerated.	9
2-2	Scanning electron micrograph (SEM) of double-heterostructure surface morphology grown on polished hydride vapor phase epitaxy (HVPE) GaN buffer.	12

LIST OF ILLUSTRATIONS (Continued)

Figure No.		Page
2-3	SEM of double-heterostructure surface morphology grown directly on (0001) sapphire.	13
2-4	SEM of double-heterostructure surface morphology grown on unpolished (as-grown) HVPE GaN buffer.	13
2-5	Transversely optically pumped edge emission output energy as a function of normalized pump pulse energy at 77 and 300 K for double heterostructure grown on polished HVPE GaN buffer. The cavity is 65 μm long, with saw-cut facets.	14
2-6	Emission spectrum at 77 K of cavity 23 μm long, with saw-cut facets. The vertical dashed lines indicate mode positions; the mode spacing is 0.56 nm.	14
2-7	(a) Transversely pumped edge emission output energy as a function of normalized pump pulse energy at 77 K for double heterostructure grown on unpolished HVPE GaN buffer. The cavity is 1 mm long, with cleaved facets. (b) Laser structure.	15
2-8	Emission spectrum at threshold (E_p = 0.14 mJ/cm^2) and above threshold (E_p = 0.38 mJ/cm^2) for double heterostructure, shown in Figure 2-8, grown on unpolished HVPE GaN buffer, with cleaved facets.	16
2-9	Pulsed threshold current density vs temperature of InAsSb/InAlAsSb quantum-well diode lasers.	18
2-10	Dependence of relative differential efficiency on temperature.	19
2-11	CW power vs current of ridge-waveguide laser at several temperatures. The width and length of the laser are 8 and 1000 μm, respectively.	19
3-1	Root-mean-square surface roughness for Si(100) that has been single-point diamond machined (SPDM) as a function of depth of cut. The tool radius was 64 μm, the feed rate was 0.95 μm/rev, and the lubricating/cooling fluid was odorless mineral spirits. The data shown compare rms roughness measured by atomic force microscopy (circles) to that obtained by optical interferometry (squares). For the above data, the diamond point was traveling parallel to the <100> direction.	24
3-2	(a) SEM of Si(100) that resulted from SPDM parallel to the <100> direction. The depth of cut was 25.4 μm, the tool radius was 64 μm, and the feed rate was 0.95 μm/rev. Two machining passes were made with ~ 50 μm of material removed. (b) Atomic force microscopy image of Si(100) from SPDM parallel to the <100> direction. The conditions and amount of material removed are similar to those for the sample shown in (a).	25

LIST OF ILLUSTRATIONS (Continued)

Figure No.		Page
3-3	Depth of crystalline damage as observed by transmission electron microscopy as a function of depth of cut for Si(100) from SPDM parallel to the (a) <100> and (b) <110> directions. The two curves show the damage depth for dislocation loops (squares) and slip planes along the {111} plane (circles).	26
3-4	Schematic diagram of geometry for SPDM (reproduced in part from Ref. 4). In the diagram, f is the feed rate (m/rev), y_c is the brittle fracture damage (crack) depth, d_c is the critical depth for the brittle-to-ductile transformation, R is the tool radius, and a, b, and z are geometric parameters used to define the conditions when the brittle fracture crack depth propagates below the cut surface plane.	28
4-1	Schematic diagram of low-temperature-grown (LTG) GaAs photoconductor embedded in coplanar-waveguide transmission line. A transimpedance amplifier is used as a readout for the dc photocurrent $i_{pc}(\tau)$. The equivalent circuit models the high-frequency response of the LTG GaAs correlator (LTGGC) to an intensity pulse $I(t)$.	31
4-2	Demonstration of LTGGC used to measure dispersion on the 1-ps time scale. (a) Measured values of $i_{pc}(\tau)$ vs time delay τ for two optical pulses that have been dispersed by propagating through 43 cm of single-mode optical fiber. (b) Measured values of $i_{pc}(\tau)$ vs τ for two optical pulses that have propagated through 94 cm of fiber. The LTGGC clearly measures the increased dispersion produced by the longer fiber.	33
5-1	Plot of pixel signal amplitudes for small region of front-illuminated charge-coupled device (CCD) containing three events from α particles of 5.5 MeV incident on the device. The charge created by each particle covers several pixels and totals about 800 000 e^-.	36
5-2	Measurements of energy deposited in CCD for alpha particles from Am^{241} whose energy has been degraded by varying thicknesses of polyimide films.	37
6-1	R vs I_{rf} for first two resonant modes of resonator at temperature $T = 70$ K. The open circles are for mode 1, $f_0 = 1.8$ GHz. The solid circles are for mode 2, $f_0 = 3.6$ GHz. The inset shows a schematic view of the patterned center conductor of the resonator with Josephson junction. Not shown are the two ground planes above and below the strip.	40

LIST OF ILLUSTRATIONS (Continued)

Figure No.		Page
6-2	R vs I_{rf} for mode 1 at various temperatures as indicated in the figure. The solid lines are fits to the data by the resistively shunted Josephson-junction model. The parameters of the fits for each temperature are given in Table 6-1.	41
6-3	J_c as determined in this work from fits to the rf resistance (closed circles) compared to that determined from dc current-voltage measurements on films of similar quality as reported in Ref. 4 (open circles).	42
7-1	Typical redundant link layout. Metal 2 can be connected to metal 1 by a laser pulse at either or both of the indicated aim points.	46
7-2	Scanning electron micrograph of a typical cut site after cutting. The metal was melted by a focused laser pulse near the center of the passivation window.	47

LIST OF TABLES

Table No.		Page
3-1	Root-Mean-Square Surface Roughness of Si(100) Single-Point Diamond Machined along the <100> Direction	29
6-1	Values of I_C and R_n Used to Obtain Fits to Data	41

INTRODUCTION

1. QUANTUM ELECTRONICS

A diode-pumped, Nd:YAG laser based source of sodium resonance radiation has been developed for astronomical adaptive optics applications. The laser system produces 18–25 mJ of sodium resonance radiation per pulse, at a pulse repetition rate of 400 Hz, with a pulse duration of 150 μs, and with a spectral half-width that can be adjusted from 1 to 6 GHz.

2. ELECTROOPTICAL MATERIALS AND DEVICES

A model has been developed to estimate the scattering loss in high-dislocation-density GaN. Consideration of wavefront deformation shows that dislocation at densities of 10^{10} cm^{-2} can result in loss coefficients on the order of 10^3 cm^{-1}.

Laser emission, with well-defined cavity modes, has been demonstrated in optically pumped GaN-$Al_{0.1}Ga_{0.9}N$ double-heterostructure lasers. The laser structures were grown using an electron-cyclotron-resonance nitrogen-discharge source and gas-source molecular beam epitaxy on GaN buffers grown by hydride vapor-phase epitaxy on *c*-plane sapphire.

Strained quantum-well diode lasers emitting at ~ 3.5 μm have operated CW up to 175 K. These lasers, grown on InAs substrates, consist of compressively strained InAsSb wells, tensile-strained InAlAsSb barriers, and AlAsSb cladding layers.

3. SUBMICROMETER TECHNOLOGY

The subsurface damage produced during single-point diamond machining of silicon has been characterized. A plastic-yield zone, consisting of slip planes and dislocation networks, has been identified extending 1–3 μm below the surface.

4. HIGH SPEED ELECTRONICS

A sampling correlator has been demonstrated that can characterize subpicosecond optical pulses without using a nonlinear crystal for second-harmonic generation. The correlator exploits the ultrafast nonlinear response of a photoconductor made of low-temperature-grown GaAs, which is embedded in a coplanar-waveguide transmission line.

5. MICROELECTRONICS

A charge-coupled device (CCD) imager has been used as a charged-particle spectrometer employing alpha particles of a few million electron volts energy. The results indicate that CCDs can be useful as a diagnostic tool in studies of inertial confinement fusion and other applications involving energetic charged particles.

6. ANALOG DEVICE TECHNOLOGY

A stripline resonator technique has been used to measure the dependence on microwave current of the impedance of fabricated superconductor/normal-metal/superconductor Josephson junctions in $YBa_2Cu_3O_7$ thin films. The results are compared with predictions of a resistively shunted junction model that yields good agreement at low and intermediate values of the microwave current.

7. ADVANCED SILICON TECHNOLOGY

A novel laser connection technology has been developed that is used to produce laser-programmable gate arrays. The programming is accomplished by linking and cutting using a *Q*-switched Nd:YLF laser.

REPORTS ON SOLID STATE RESEARCH

1 NOVEMBER 1995 THROUGH 31 JANUARY 1996

PUBLICATIONS

Design Considerations for 193 nm Positive Resists	R. D. Allen* G. M. Wallraff* R. A. DiPietro* D. C. Hofer* R. R. Kunz	In *Microelectronics Technology Polymers for Advanced Imaging and Packaging, ACS Symposium Series,* Vol. 614 (American Chemical Society, Washington, D. C., 1995), p. 255
The Development of an Artificial Retina Based on Smart-Pixel and Microlens Arrays	B. Aull Z. L. Liau P. A. Maki	*IEEE Lasers and Electro-Optics Society 1995 Annual Meeting, Conference Proceedings,* Vol. 2, (IEEE, Piscataway, N.J., 1995), p. 266
GaSb-Based Mid-Infrared Semiconductor Lasers	H. K. Choi G. W. Turner H. Q. Le	*International Conference on Narrow Gap Semiconductors, Institute of Physics Conference Series,* No. 144, Sec. 1 (Institute of Physics Publishing, Bristol, U.K., 1995), p. 1
Room-Temperature 50-mJ/Pulse Side-Diode-Pumped Yb:YAG Laser	D. S. Sumida* T. Y. Fan	*Opt. Lett.* **20**, 2384 (1995)
Plasma-Deposited Silylation Resist for 193 nm Lithography	M. W. Horn M. Rothschild B. E. Maxwell R. B. Goodman R. R. Kunz L. M. Eriksen	*Appl. Phys. Lett.* **68**, 179 (1996)

*Author not at Lincoln Laboratory.

Top-Surface Imaged Resist Processes for 193-nm Lithography	R. R. Kunz S. C. Palmateer A. R. Forte M. W. Horn M. Rothschild	In *Microelectronics Technology Polymers for Advanced Imaging and Packaging, ACS Symposium Series,* Vol. 614 (American Chemical Society, Washington, D.C., 1995), p. 271
High Power Diode-Laser-Pumped Midwave Infrared HgCdTe/CdZnTe Quantum Well Lasers	H. Q. Le A. Sanchez J. M. Arias* M. Zandian* R. R. Zucca* Y.-Z. Liu*	*International Conference on Narrow Gap Semiconductors, Institute of Physics Conference Series,* No. 144, Sec. 1 (Institute of Physics Publishing, Bristol, U.K., 1995), p. 24
Fabrication of Two-Sided Anamorphic Microlenses and Direct Coupling of Tapered High-Power Diode Laser to Single-Mode Fiber	Z. L. Liau J. N. Walpole J. C. Livas E. S. Kintzer D. E. Mull L. J. Missaggia W. F. DiNatale	*IEEE Photon. Technol. Lett.* **7**, 1315 (1995)
Auger Lifetime in InAs, InAsSb, and InAsSb-InAlAsSb Quantum Wells	J. R. Lindle* J. R. Meyer* C. A. Hoffman* F. J. Bartoli* G. W. Turner H. K. Choi	*Appl. Phys. Lett.* **67**, 3153 (1995)
Nonlinear Surface Impedance of YBCO Thin Films: Measurements, Modeling, and Effects in Devices	D. E. Oates P. P. Nguyen G. Dresselhaus* M. S. Dresselhaus* G. Koren* E. Polturak*	*J. Superconduct.* **8**, 725 (1995)

*Author not at Lincoln Laboratory.

Microwave Power Dependence of $YBa_2Cu_3O_7$ Thin-Film Josephson Edge Junctions	D. E. Oates P. P. Nguyen Y. Habib* G. Dresselhaus* M. S. Dresselhaus* G. Koren* E. Polturak*	*Appl. Phys. Lett.* **68**, 705 (1996)
Profile Control in Dry Development of High-Aspect-Ratio Resist Structures	M. B. Stern S. C. Palmateer M. W. Horn M. Rothschild B. E. Maxwell J. E. Curtin	*J. Vac. Sci. Technol. B* **13**, 3017 (1995)
Analysis of Multiple Input N×M Waveguide Couplers with Multimode Guiding Sections	E. R. Thoen* L. A. Molter* J. P. Donnelly	*Conference on Lasers and Electro-Optics, 1995 Technical Digest Series,* Vol. 15 (Optical Society of America, Washington, D.C., 1995), p. 301
n-AlGaSb and GaSb/AlGaSb Double-Heterostructure Lasers Grown by Organometallic Vapor Phase Epitaxy	C. A. Wang K. F. Jensen* A. C. Jones* H. K. Choi	*Appl. Phys. Lett.* **68**, 400 (1996)

*Author not at Lincoln Laboratory.

ACCEPTED FOR PUBLICATION

Optically Pumped $GaN/Al_{0.1}Ga_{0.9}N$ Double-Heterostructure Ultraviolet Laser	R. L. Aggarwal P. A. Maki R. J. Molnar Z. L. Liau I. Melngailis	*J. Appl. Phys.*
Mid-Infrared Lasers Fabricated from III-V Compound Semiconductors	H. K. Choi	*Current Opinion Solid State Mater. Sci.*
Generalized Effective Index Series Solution Analysis of Waveguide Structures with Positionally Varying Refractive Index Profiles	J. P. Donnelly S. D. Lau*	*J. Quantum Electron.*
Nondegenerate Four-Wave Mixing Wavelength Conversion in Low-Loss Passive InGaAsP/InP Quantum-Well Waveguides	J. P. Donnelly H. Q. Le E. A. Swanson S. H. Groves	*IEEE Photon. Technol. Lett.*
Diode-Pumped Solid-State Lasers	T. Y. Fan	In *New Perspectives in Laser Sources and Applications* (Institute of Physics Publishing, Philadelphia, Pa.)
Surface Vapor Transport for Accurate Microoptics in Compound Semiconductors	Z. L. Liau	*Mater. Chem. Phys.*
A 9-Bit Charge-to-Digital Converter for Integrated Image Sensors	S. A. Paul H-S. Lee*	*Electron. Design*
193-nm Lithography	M. Rothschild	*IBM J. Res. Dev.*

*Author not at Lincoln Laboratory.

In-Situ Concentration Monitoring in a Vertical OMVPE Reactor by Fiber Optics Based Fourier Transform Infrared Spectroscopy	S. Salim* C. A. Wang R. D. Driver* K. F. Jensen*	*J. Cryst. Growth*
Microwave Intermodulation Products and Excess Critical Current in $YBa_2Cu_3O_{7-x}$ Josephson Junctions	T. C. L. G. Sollner J. P. Sage D. E. Oates	*Appl. Phys. Lett.*
Semiconductor Amplifiers and Lasers with Tapered Gain Regions—A Tutorial Review	J. N. Walpole	*Opt. Quantum Electron.*
Low Oxygen and Carbon Incorporation in AlGaAs Using Tritertiarybutylaluminum in Organometallic Vapor Phase Epitaxy	C. A. Wang S. Salim* K. F. Jensen* A. C. Jones*	*J. Electron. Mater.*
Passively *Q*-Switched Microchip Lasers	J. J. Zayhowski	*Laser Focus World*
UV Generation with Passively *Q*-Switched Microchip Lasers	J. J. Zayhowski	*Opt. Lett.*
Miniature Solid-State Lasers	J. J. Zayhowski J. Harrison	In *CRC Handbook of Electro-optics* (CRC Press, Boca Raton, Fla.)

*Author not at Lincoln Laboratory.

PRESENTATIONS†

Diamond Cold Cathodes: Experiment and Theory	M. W. Geis J. C. Twichell T. M. Lyszczarz K. E. Krohn N. N. Efremow C. A. Marchi	Technical Seminar, SI Diamond, Inc., Austin, Texas, 1 November 1995
Antimonide-Based Semiconductor Laser for 2–5 μm Emission	H. K. Choi	Lincoln Laboratory Technical Seminar Series, University of California, Berkeley, California, 3 November 1995
Diamond Electronics	M. W. Geis	Lincoln Laboratory Technical Seminar Series, Rice Quantum Institute, Houston, Texas, 3 November 1995; Massachusetts Institute of Technology, Cambridge, Massachusetts, 11 January 1996
Optical Link for Cellular Telephone Microcells	G. E. Betts	MILCOM '95, San Diego, California, 8 November 1995
Nonlinear Microwave Flux Dynamics: Relationship Between Pinning and Power Dependence	N. Belk* D. E. Oates G. Dresselhaus* M. S. Dresselhaus*	1995 Fall Meeting of the Materials Research Society, Boston, Massachusetts, 27 November– 1 December 1995
Analysis of Frequency Dependence of Vortex Dynamics in $YBa_2Cu_3O_{7-\delta}$ Thin Films in DC Magnetic Field	N. Belk* D. E. Oates D. A. Feld G. Dresselhaus* M. S. Dresselhaus*	

*Author not at Lincoln Laboratory.

†Titles of presentations are listed for information only. No copies are available for distribution.

Electron Emission from Diamond	M. W. Geis J. C. Twichell T. M. Lyszczarz K. E. Krohn N. N. Efremow C. A. Marchi	1995 Fall Meeting of the Materials Research Society, Boston, Massachusetts, 27 November–1 December 1995
DC Magnetic Field Effects on the Microwave Power Dependence of $YBa_2Cu_3O_{7-x}$ Thin-Film Josephson Edge Junctions	Y. M. Habib* D. E. Oates G. Dresselhaus* M. S. Dresselhaus* G. Koren* E. Polturak*	
Optically Pumped GaN-AlGaN Double-Heterostructure Lasers Grown by ECR-GSMBE and HVPE	P. A. Maki R. J. Molnar R. L. Aggarwal Z. L. Liau I. Melngailis	
Optoelectronic and Structural Properties of High Quality GaN Grown by Hydride Vapor Phase Epitaxy	R. J. Molnar E. R. Brown R. Aggarwal Z. L. Liau I. Melngailis	
Highly Functional 2-D MESFET/RTD Logic Element for Low-Power Applications	E. R. Brown J. Robertson* T. Ytterdal* W. C. B. Peatman*	1995 International Semiconductor Device Research Symposium, Charlottesville, Virginia, 6-8 December 1995
GaSb-Based Mid-Infrared Quantum-Well Diode Lasers	H. K. Choi G. W. Turner	
Correlation of Optical Pulses with a Low-Temperature-Grown GaAs Photoconductor	S. Verghese N. Zamdmer* E. R. Brown A. Forster*	

*Author not at Lincoln Laboratory.

193-nm Lithography	M. Rothschild A. R. Forte M. W. Horn R. R. Kunz S. C. Palmateer J. H. C. Sedlacek	Semiconductor Equipment and Materials International Technology Symposium, Chiba, Japan, 6-8 December 1995
Electronic Applications of Superconducting Thin Films	A. C. Anderson	Lincoln Laboratory Technical Seminar Series, Massachusetts Institute of Technology, Cambridge, Massachusetts, 14 December 1995
Photoimaging Processes for Use at 193 nm and Their Application to Sub-quarter Micrometer Device Manufacturing	R. R. Kunz	1995 International Chemical Congress of the Pacific Basin Society, Honolulu, Hawaii, 17-22 December 1995
Semiconductor Laser Microoptics: Fabrication, Packaging and Analysis	Z. L. Liau	Lincoln Laboratory Technical Seminar Series, University of Minnesota, Minneapolis, Minnesota, 25 January 1996

Antimonide-Based Quantum-Well Diode Lasers Emitting Beyond 3 μm	H. K. Choi G. W. Turner M. J. Manfra M. K. Connors F. P. Herrmann A. Baliga* N. G. Anderson*	SPIE Symposium on Lasers and Integrated Electronics, San Jose, California, 27 January–2 February 1996
High Resolution Heterodyne Spectroscopy Using GaAs/AlGaAs MQW Detectors	K. A. McIntosh E. R. Brown K. B. Nichols	
193-nm Lithography	M. Rothschild A. R. Forte M. W. Horn R. R. Kunz S. C. Palmateer J. H. C. Sedlacek	

*Author not at Lincoln Laboratory.

ORGANIZATION

SOLID STATE DIVISION

D. C. Shaver, *Head*
I. Melngailis, *Associate Head*
R. W. Ralston, *Associate Head*
J. F. Goodwin, *Assistant*

A. L. McWhorter, *Fellow*
C. L. Keast, *Staff*
D. Abusch-Magder, *Research Assistant*
J. T. Chiou, *Research Assistant*
J. P. Mattia, *Research Assistant*
N. L. DeMeo, Jr., *Associate Staff*
J. W. Caunt, *Assistant Staff*
K. J. Challberg, *Administrative Staff*

SUBMICROMETER TECHNOLOGY

M. Rothschild, *Leader*
T. M. Lyszczarz, *Assistant Leader*
L. H. Dubois, *Senior Staff*†

Astolfi, D. K.
Bloomstein, T. M.
Craig, D. M.
DiNatale, W. F.
Doran, S. P.
Efremow, N. N., Jr.
Forte, A. R.
Geis, M. W.
Goodman, R. B.
Hartney, M. A.
Horn, M. W.
Kunz, R. R.
Liu, H. I.
Maki, P. A.
Palmateer, S. C.
Reinold, J. H., Jr.
Sedlacek, J. H. C.
Stern, M. B.
Twichell, J. C.
Uttaro, R. S.

QUANTUM ELECTRONICS

A. Sanchez-Rubio, *Leader*
T. Y. Fan, *Assistant Leader*

Aggarwal, R. L.
Cook, C. C.
Daneu, V.
DeFeo, W. E.
DiCecca, S.
Dill, C., III
Jeys, T. H.
Le, H. Q.
Ochoa, J. R.
Zayhowski, J. J.

ELECTROOPTICAL MATERIALS AND DEVICES

B. Y. Tsaur, *Leader*
D. L. Spears, *Assistant Leader*
R. C. Williamson, *Senior Staff*

Bailey, R. J.
Betts, G. E.
Chen, C. K.
Choi, H. K.
Connors, M. K.
Donnelly, J. P.
Foley, L. J.*
Goodhue, W. D.
Groves, S. H.
Harman, T. C.
Herrmann, F. P.
Hovey, D. L.
Iseler, G. W.
Krohn, L., Jr.
Liau, Z. L.
Manfra, M. J.
McGilvary, W. L.
Missaggia, L. J.
Mull, D. E.
Napoleone, A.
Nee, P.*
Nitishin, P. M.
O'Donnell, F. J.
Palmacci, S. T.
Paul, S. A.*
Poillucci, R. J.
Reeder, R. E.
Santiago, D. D.
Tsang, D. Z.
Turner, G. W.
Walpole, J. N.
Wang, C. A.

* Research Assistant
† Intergovernmental Personnel Act assignment

HIGH SPEED ELECTRONICS

M. A. Hollis, *Leader*
E. R. Brown, *Assistant Leader*
R. A. Murphy, *Senior Staff*

Bozler, C. O.
Chen, C. L.
Harris, C. T.
Lincoln, G. A., Jr.
Mahoney, L. J.
Mathews, R. H.
McIntosh, K. A.
McMahon, O. B.
Molnar, R. J.
Rabe, S.
Rathman, D. D.
Verghese, S.

ANALOG DEVICE TECHNOLOGY

T. C. L. G. Sollner, *Leader*
L. M. Johnson, *Assistant Leader*
A. C. Anderson, *Senior Staff*

Arsenault, D. R.
Boisvert, R. R.
Brogan, W. T.
Donahue, K. G.
Feld, D. A.
Fitch, G. L.
Gleason, E. F.
Hamm, J. M.
Holtham, J. H.
Lyons, W. G.
Macedo, E. M., Jr.
McClure, D. W.
Murphy, P. G.
Oates, D. E.
Sage, J. P.
Seaver, M. M.
Slattery, R. L.

MICROELECTRONICS

E. D. Savoye, *Leader*
B. B. Kosicki, *Associate Leader*
B. B. Burke, *Senior Staff*

Aull, B. F.
Clark, H. R., Jr.
Daniels, P. J.
Doherty, C. L., Jr.
Dolat, V. S.
Donahue, T. C.
Felton, B. J.
Gregory, J. A.
Hotaling, T. C.
Johnson, K. F.
Lind, T. A.
Loomis, A. H.
McGonagle, W. H.
Mountain, R. W.
Percival, K. A.
Reich, R. K.
Young, D. J.

ADVANCED SILICON TECHNOLOGY

J. I. Raffel, *Leader*
P. W. Wyatt, *Associate Leader*
A. H. Anderson, *Senior Staff*

Berger, R.
Burns, J. A.
Davis, P. V.
D'Onofrio, R. P.
Frankel, R. S.
Fritze, M.
Herndon, T. O.
Howard, J. F.
Knecht, J. M.
Newcomb, K. L.
Soares, A. M.
Wachtmann, B. K.
Young, G. R.

1. QUANTUM ELECTRONICS

1.1 Nd:YAG SUM-FREQUENCY SOURCE OF SODIUM-RESONANCE RADIATION

A diode-pumped, Nd:YAG laser based source of sodium-resonance radiation has been developed for astronomical adaptive optics applications [1]. The laser system produces 18–25 mJ of sodium-resonance radiation per pulse at a pulse repetition rate of 400 Hz, with a pulse duration of 150 μs, and with a spectral half-width that can be adjusted from 1 to 6 GHz. The laser system was installed in December 1995 at the 3.5-m-aperture telescope at Apache Point, New Mexico, for use by the University of Chicago.

A schematic of the laser system is shown in Figure 1-1. The laser system is composed of a 1064-nm Nd:YAG oscillator, a 1319-nm Nd:YAG oscillator, laser beam handling optics, and a dual-crystal sum-frequency mixing apparatus. Each Nd:YAG laser contains a diode-pumped Nd:YAG zigzag head (one for the 1064-nm laser and two for the 1319-nm laser), an acoustooptic mode-locker crystal, a nonlinear second-harmonic-generation crystal for spiking suppression [2], and an etalon for tuning the wavelength of the laser radiation.

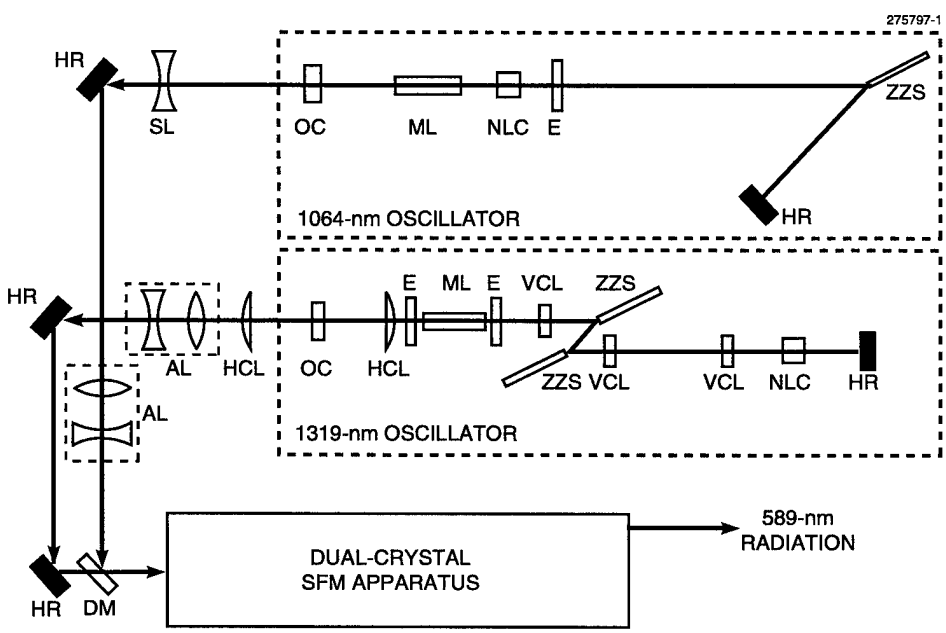

Figure 1-1. Schematic of laser system. The abbreviations shown in the figure are as follows: HR, high reflector; ZZS, zigzag slab; E, etalon; NLC, nonlinear crystal; ML, mode locker; OC, output coupler; VCL, vertical cylindrical lens; HCL, horizontal cylindrical lens; AL, adjustable spherical lens; SL, spherical lens; DM, dichroic mirror. The dual-crystal sum-frequency mixing apparatus is shown in Figure 1-3.

The laser head, shown schematically in Figure 1-2, contains a diode laser module consisting of four pairs of square-centimeter diode arrays [3] arranged in a 2 × 4 configuration. A cylindrical lens array (not shown) is cemented in front of each diode array in order to collimate the high divergence component of the diode laser radiation. The radiation from each pair of diodes passes through a separate cylindrical lens which focuses the collimated dimension of the radiation beyond the position of the Nd:YAG zigzag slab. The diode radiation converges into the slab in the dimension perpendicular to its long axis and slightly diverges in the dimension parallel to its long axis. By individually translating each of the four cylindrical lenses, the transverse position of the radiation in the slab can be adjusted to control the transverse gain profile and the diode-pump-induced thermal lens in the slab.

Because the laser radiation travels through the Nd:YAG slab along a zigzag path, the diode-pump-induced thermal lens acts only transversely to the plane of the zigzag path. This asymmetry in the effective thermal lens causes the laser cavities to be different in the two orthogonal dimensions parallel and perpendicular to the plane of the zigzag path. In the plane parallel to the zigzag path (plane of the page in Figure 1-1), the 1064-nm beam parameters are determined by the flat output coupler, the cylindrical concave high reflector mirror, and the cavity length. The curvature of the high reflector is adjusted for single transverse mode laser operation with the slab input/output surface forming the transverse mode selection aperture. Thus, between the cylindrical high reflector and the output coupler, the beam slowly

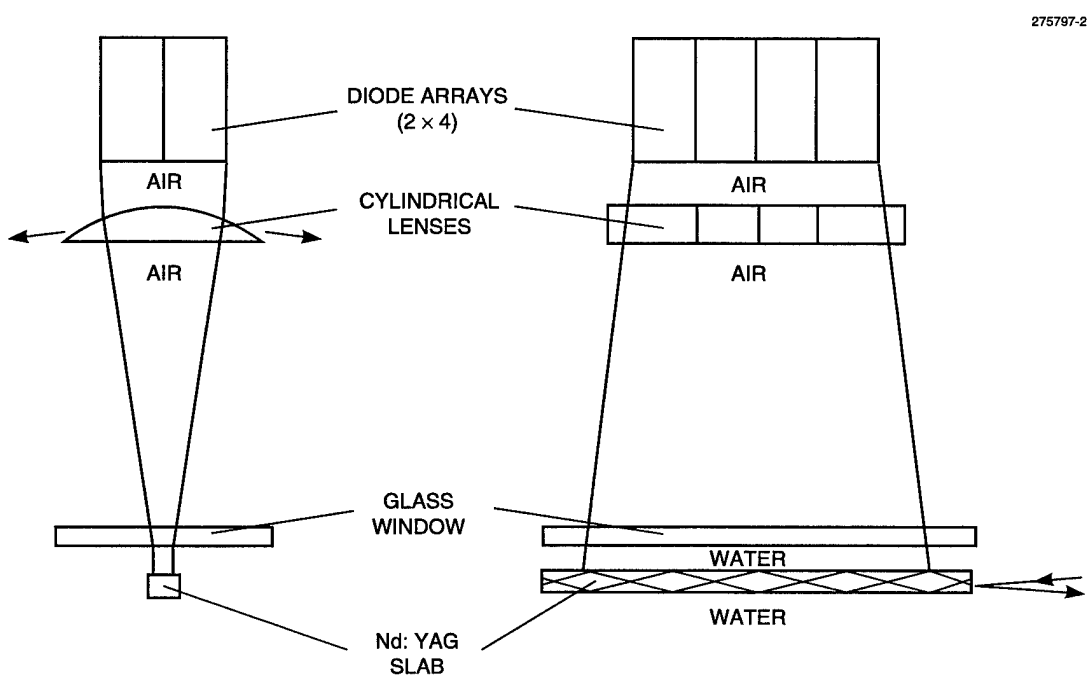

Figure 1-2. Schematic of diode-pumped, Nd:YAG, zigzag laser head. The path of the laser radiation inside the slab is shown to traverse a five-diamond path. The input surface is antireflection coated at the laser wavelength. The end surface is high-reflection coated at the laser wavelength, and for the 1319-nm laser this end is high-transmission coated for 1064-nm radiation. The Nd:YAG slab is 5.5 cm long, 2.5 cm thick, and 3.5 cm wide.

decreases in size to a waist on the output coupler. In the plane perpendicular to the zigzag path, the laser beam parameters are determined by the flat output coupler, the slab thermal lens, the flat (in this dimension) high reflector, and the cavity length. Between the output coupler and the slab, the beam is nominally collimated with a beam waist on the output coupler. Between the slab and the high reflector, the beam size decreases to a line focus on the high reflector. The optical cavity of the 1319-nm laser is substantially different from the 1064-nm cavity because it contains two laser heads and because it is compensated by a transverse beam instability. As for the 1064-nm laser cavity, the 1319-nm cavity is different for the two transverse dimensions, parallel and perpendicular to the plane of the Nd:YAG zigzag path. Two negative-focal-length cylindrical lenses are placed in the 1319-nm cavity, on either side of the two laser heads, in order to compensate for the diode-pump-induced thermal lenses. In addition to this thermal lens, there is also a thermal lens created by laser action at 1319 nm. Because the 1319-nm photon carries away less energy than an average fluorescence photon, laser operation at 1319 nm generates a thermal lens along the laser beam path which is not compensated at all by the zigzag path in the slab. The 1319-nm thermal lens causes the transverse position of the 1319-nm beam to be unstable, which results in a very severe power instability and makes alignment of the cavity for optimum power nearly impossible. The transverse beam position is restabilized by the addition of two cylindrical lenses in the cavity, which create cat-eye reflections of the laser beam at the output coupler and the high reflector in orthogonal planes. A cylindrical lens after the 1319-nm output coupler makes the laser beam have a near circular transverse beam profile.

The acoustooptic mode lockers in each Nd:YAG laser are driven by a common RF generator to assure identical 100-MHz mode locking of each laser cavity. The temporal phase of the mode-locked pulses is controlled by adjusting the relative phase of the RF power driving the mode lockers. The antireflection-coated, 1-cm-long, intracavity lithium iodate crystals are used to suppress the relaxation oscillations through second-harmonic generation. The lasers are tuned using etalons in each laser cavity. The 1319-nm cavity contains a 30%-reflecting-per-surface, 2-mm-thick etalon which is angularly tuned for maximum power from the 1319-nm laser. The 1064-nm cavity contains a 60%-reflecting-per-surface, 1-mm-thick etalon which is angularly tuned so that the sum-frequency radiation is resonant with the sodium $3S_{1/2} - 3P_{3/2}$ (D_2) transition as observed in a sodium vapor cell.

The outputs of both the 1064- and 1319-nm lasers are passed through beam conditioning optics so that the confocal parameter of each beam is about the same and focuses to the same position in the nonlinear crystals. The 1064- and 1319-nm laser beams are superimposed and made to propagate in the same direction by a dichroic mirror which reflects the 1064-nm beam and transmits the 1319-nm beam. The combined beams are focused by a 15-cm-focal-length lens into a lithium triborate crystal ($3 \times 3 \times 18$ mm) which is antireflection coated at 589, 1064, and 1319 nm, as seen in Figure 1-3. After passing through the crystal the radiation is reflected, at near normal incidence, from a concave high reflector (at all three wavelengths) through a pair of phase compensating glass wedges and into a second lithium triborate crystal. The concave mirror refocuses the radiation into the second crystal with the same beam parameters as in the first crystal [4]. The phase compensating wedges can be adjusted to compensate for air dispersion and rephase the 589-nm radiation generated in the first crystal with the 589-nm radiation generated in the second crystal. When the wedges are adjusted for constructive interference, substantially more sum radiation exits the second crystal than the first crystal. When the wedges are

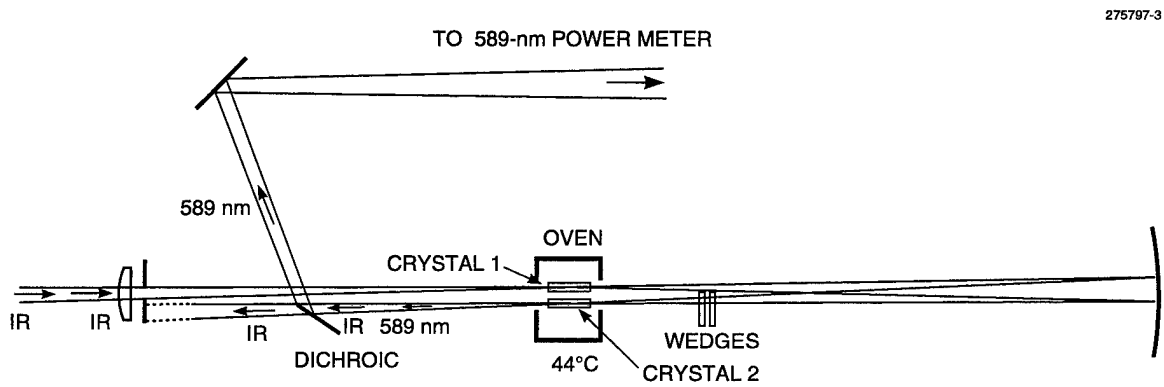

Figure 1-3. Schematic of dual-crystal sum-frequency mixing apparatus. The dichroic mirror has high reflectivity at 589 nm for s-polarization light and high transmissivity at 1064 and 1319 nm for p-polarization light.

adjusted for destructive interference, substantially less sum radiation exits the second crystal than the first crystal. Finally, the 589-nm radiation is separated from the 1064- and 1319-nm radiation by two dichroic mirrors after the second nonlinear crystal.

The diode pump lasers operate at a pulse repetition rate of 400 Hz and with a pump pulse duration of 200 μs. The output power of the Nd:YAG lasers depends on the selectivity of the intracavity etalons. By using etalons that restrict the 1064- and 1319-nm lasers to spectral widths of 1.7 and 1.2 GHz, respectively, the lasers have pulse durations of 170 and 145 μs, respectively, and generate 12.75 and 10 W of average power. The temporal profiles of the mode-locked pulse envelope, and the mode-locked pulses themselves, are shown in Figures 1-4 and 1-5. As can be seen, nearly 50% depletion of the Nd:YAG radiation is achieved. Sum-frequency mixing of this radiation generates 8.25 W of average sodium-resonance radiation power (36% conversion efficiency) with a spectral width of 0.94 GHz. The spectral width of the sum radiation, in this case, was narrower than either laser because the mode-locked pulses from each laser were frequency chirped in opposite directions. The direction of chirping for each Nd:YAG laser was controlled by the angle of the acoustooptic crystal relative to the intracavity laser beam. When the 1064- and 1319-nm pulses were chirped in the same direction, the spectral width of the sum radiation was substantially greater than when the chirps were in opposite directions.

T. H. Jeys
V. Daneu

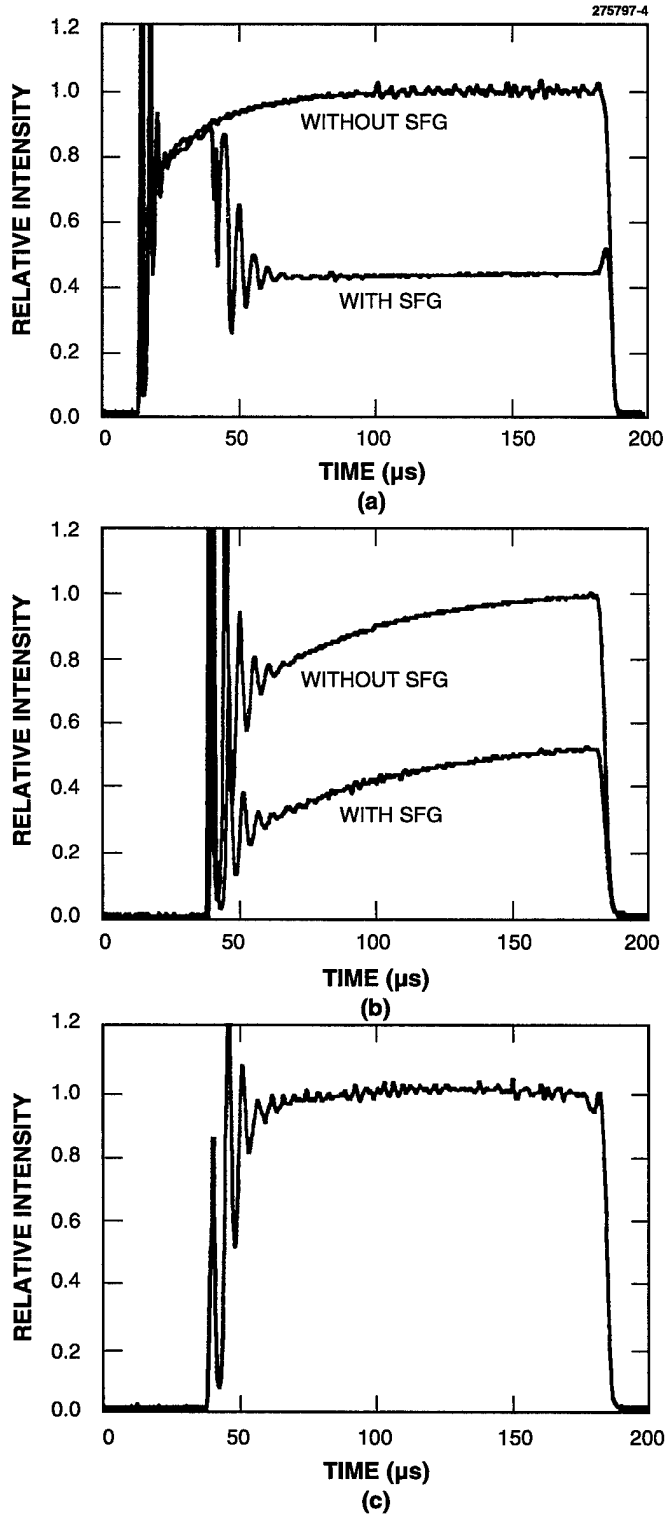

Figure 1-4. Temporal envelopes of (a) 1064-, (b) 1319-, and (c) 589-nm mode-locked pulse train after passing through frequency mixing apparatus. The profiles with and without sum-frequency generation (SFG) were obtained by adjusting the relative timing of the mode-locked pulses so that there either was or was not temporal overlap of the pulses in the nonlinear crystals. Note that the 1064-nm laser pulse has a longer duration than the 1319-nm pulse. The diode pump radiation has a duration of 200 μs with the end of the Nd:YAG laser radiation marking the end of the diode pump radiation.

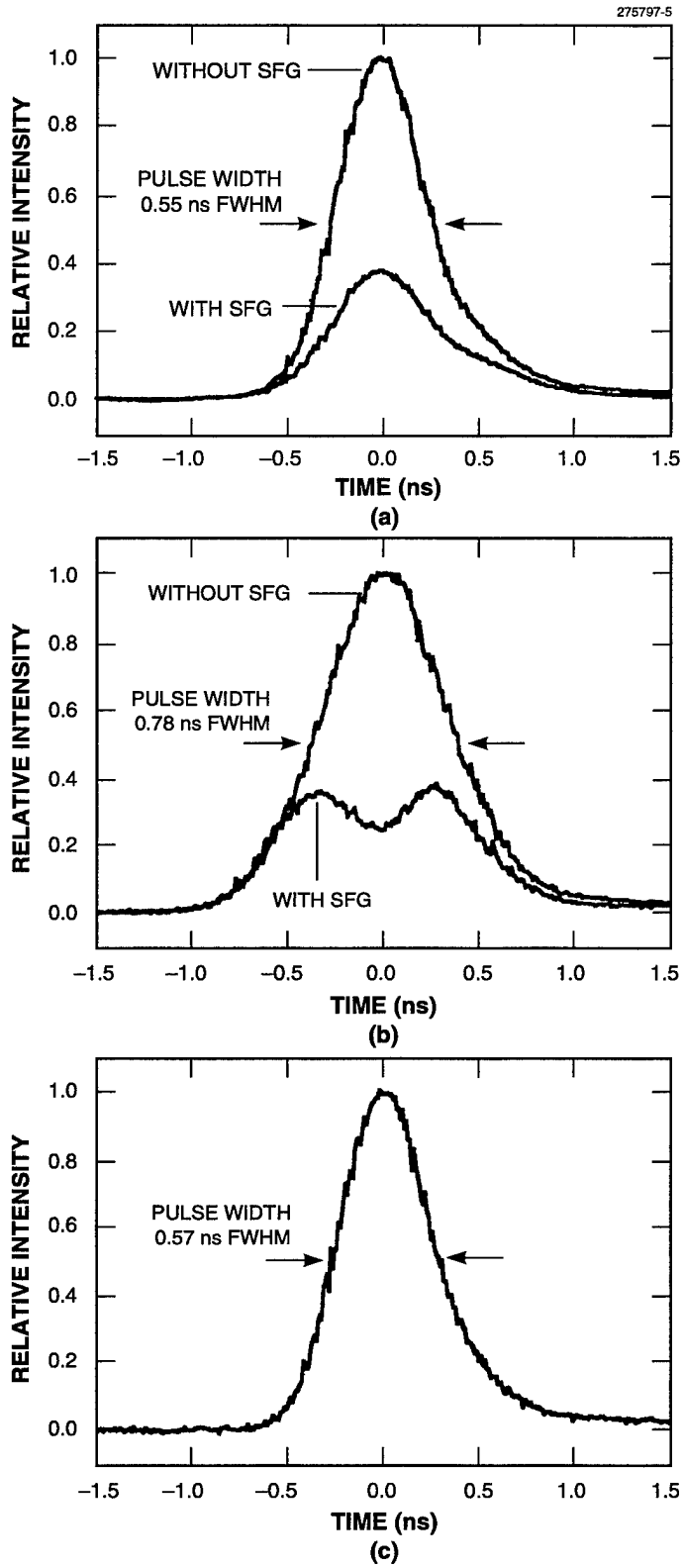

Figure 1-5. Temporal profiles of the (a) 1064-, (b) 1319-, and (c) 589-nm mode-locked pulses after passing through frequency mixing apparatus. Profiles with and without SFG were obtained as described in Figure 1-4.

REFERENCES

1. R. A. Humphreys, C. A. Primmerman, L. C. Bradley, and J. Herrmann, *Opt. Lett.* **16**, 1367 (1991); C. A. Primmerman, D. V. Murphy, D. A. Page, B. G. Zollars, and H. T. Barclay, *Nature* **353**, 141 (1991); R. Q. Fugate, D. L. Fried, G. A. Ameer, B. R. Boeke, S. L. Browne, P. H. Roberts, R. E. Ruane, G. A. Tyler, and L. M. Wopat, *Nature* **353**, 144 (1991); T. H. Jeys, *Lincoln Laboratory J.* **4**, 133 (1991).
2. T. H. Jeys, *Appl. Opt.* **30**, 1011 (1991).
3. Product number SDL-3235-J5, SDL, Inc., San Jose, California.
4. Solid State Research Report, Lincoln Laboratory, MIT, 1994:2, p. 18.

2. ELECTROOPTICAL MATERIALS AND DEVICES

2.1 LIGHT SCATTERING IN HIGH-DISLOCATION-DENSITY GaN

There has been considerable recent interest in nitride-based blue and ultraviolet light-emitting diodes (LEDs) and lasers, for display, storage, and spectroscopic applications. Relatively efficient and reliable blue LEDs have been developed [1],[2]. The laser development, however, is still at an early stage and efficient lasers have not been reported. Initial results indicate that lasers suffer from high propagation loss in the lasing medium. This loss may be due to scattering of the lightwave, either from imperfect surface morphology or from dislocations within the material. Advances in growth technology to improve morphology are addressed in Section 2.2.

Here, we focus on the scattering loss induced by dislocations. Current nitride materials show very high dislocation densities [3],[4], typically 2–10 $\times$ 10^{10} cm^{-2}, which may give rise to significant light scattering. This scattering would not degrade the efficiency of an LED, but would induce a significant scattering loss in a laser structure. In this work we describe a simple model to estimate this loss and show that the high dislocation density can indeed give rise to significant high loss coefficient.

Consider a typical nitride layer or layer structure. Edge dislocations with lines perpendicular to the layer have been predominantly observed [3],[4] and are modeled here. Figure 2-1 illustrates the model for the effect of a single edge dislocation. In this illustration, the page is parallel to the layer in which the lightwave propagates. The dislocation's extra plane of atoms in the upper-half region increases the optical length and delays the wave propagation there. In this simple model, we estimate the optical-path-length difference δ by

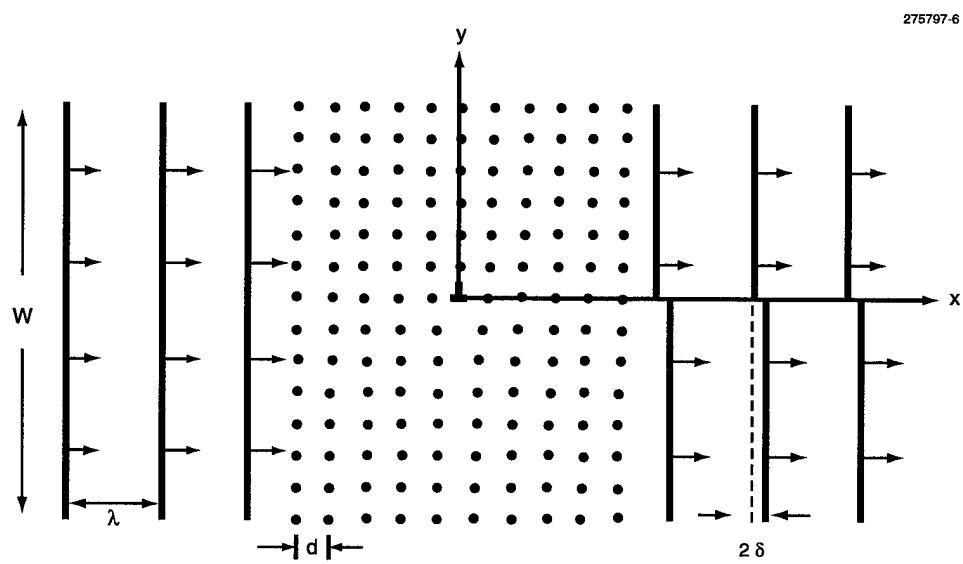

Figure 2-1. Model of lightwave scattering by dislocation, where thick lines indicate wavefronts and dots indicate atoms in the crystal lattice. The extra plane of atoms in the upper region results in a phase delay in that portion of the wavefront. The wavefront deformation then gives rise to scattering loss. Note that the figure is not drawn to scale; the wavelength λ should be much greater than the atomic spacing d. The path length difference δ is also greatly exaggerated.

using the product of the refractive index n of GaN and the thickness of one atomic layer d, that is,

$$\delta \cong nd \ . \tag{2.1}$$

Since this represents a very small wavefront deformation (i.e., δ is much smaller than the wavelength λ), the resulting loss is given by the mean square of this deformation [5], that is,

$$\frac{\Delta I}{I} \cong -\left(\frac{1}{2}\frac{2\pi\delta}{\lambda}\right)^2 \ , \tag{2.2}$$

where I and ΔI are the beam intensity and the change in beam intensity, respectively. This simplified calculation assumes an edge dislocation at the center of the beam with the missing plane of atoms parallel to the wavefront. A more detailed calculation for randomly placed dislocations with planes of missing atoms at other angles is under way.

As the lightwave travels along the layer it encounters other dislocations, and the overall loss per unit length becomes the loss coefficient. With randomly distributed dislocations the overall loss can be obtained by adding the individual ones, and the loss coefficient α is given by

$$\alpha \cong \left(\frac{\pi\delta}{\lambda}\right)^2 Nw \ , \tag{2.3}$$

where N is the dislocation density per unit area and w is the lateral extent of the wave. The attenuation has a beamwidth dependence because the probability of encountering an edge dislocation is width dependent. In the present stage of broad-area laser development (without strong lateral index guiding), the parameter w can be taken as the width of each lasing filament. Note that Equation (2.3), in combination with Equation (2.1), expresses the loss coefficient in terms of the basic parameters n, d, N, λ, and w.

To estimate the magnitude of the loss coefficient α for GaN with $N = 2 \times 10^{10}$ cm^{-2}, we use n = 2.7, d = 3 Å, λ = 0.36 μm, and $w \approx 10$ μm. (This w value is an estimated lateral mode extent.) This yields

$$\alpha \cong 1\times10^3 \text{cm}^{-1} \ , \tag{2.4}$$

which indicates that significant large loss coefficients can indeed result from very high dislocation densities.

Although this estimated loss coefficient seems to be consistent with the apparent low laser differential quantum efficiencies [6],[7], more quantitative comparison is not possible at the present time. Other scattering mechanisms such as nonideal surface and interface morphologies can also give rise to considerable scattering losses. The present model nevertheless provides a way to estimate the loss caused by dislocations and shows that significant scattering losses can result from very high dislocation densities. The model suggests that the dislocation density needs to be lowered by at least two orders of magnitude in order to achieve lasers of good external efficiency. Recent advancement of hydride vapor phase epitaxy has resulted in GaN layers with dislocation densities as low as 3×10^8 cm^{-2} [8].

Z. L. Liau
R. L. Aggarwal
P. A. Maki
R. J. Molnar
I. Melngailis

2.2 OPTICALLY PUMPED GaN-AlGaN DOUBLE-HETEROSTRUCTURE LASERS GROWN BY ECR-MBE AND HVPE

The demonstration of efficient LEDs in the group III–nitride material system [9] indicates that there is an excellent prospect for realizing diode lasers that span the visible to the ultraviolet. This would enable many low-cost applications based on diode lasers, such as optical data recording/reading, chemical sensing, and displays. While the development of efficient, long-lived diode lasers in this wavelength range is the eventual objective, optical pumping is a convenient technique for evaluating the optical properties of GaN laser structures without the added complications posed by electrical injection. Optically pumped lasing has been demonstrated [10],[11], and there have been a number of reports of stimulated emission [12]–[16]; however, high threshold power densities observed in the optical pumping experiments indicate that the realization of a low threshold current density diode laser will require improvements in the material and laser structures.

The gain characteristics of GaN lasers are intimately dependent on the substrate used for epitaxial growth and on the growth technique. Variations of these affect both the surface morphology and the dislocation density of the epitaxial films. A potential limiting factor in the performance of GaN lasers is loss of the optical mode as it is guided through the lasing medium. Imperfect morphology and high dislocation densities can both lead to scattering loss. Section 2.1 focused on estimating the loss contributed by dislocations.

The observed length scale of surface ripple of GaN heteroepitaxially grown directly on (0001) sapphire by electron cyclotron resonance molecular beam epitaxy (ECR-MBE) can contribute to high scattering losses in the guided mode for GaN/AlGaN double heterostructures in the ultraviolet wavelength range. Here, we demonstrate that the morphology of the epitaxial GaN film can be improved by using a GaN buffer grown by hydride vapor phase epitaxy (HVPE) on (0001) sapphire as the starting substrate. The advantage of the HVPE buffer is that the morphology is optically smoother in the ultaviolet than for GaN material grown by ECR-MBE on sapphire using a low-temperature buffer (two-step process). The HVPE buffer enables homoepitaxial growth which replicates the starting surface morphology. The morphology of the HVPE buffer at present exhibits a variety of growth features characteristic of the HVPE process, but by mechanically polishing these buffers, high-quality, planar surfaces can be obtained. It should be noted, however, that stimulated emission is observed from layers grown on both as-grown and polished surfaces. Using these buffers, we have observed, for the first time, optically pumped laser emission exhibiting cavity modes in GaN/AlGaN double heterostructures grown by ECR-MBE.

The details of the HVPE process have been published elsewhere [17]. The HVPE buffers, initially ~ 15 μm in thickness, grown on (0001) sapphire, are mechanically polished to remove growth hillocks, with a resulting thickness of ~ 8 μm. The MBE system is a Varian gas-source modular GEN II. Effusion sources are used for elemental gallium and aluminum. The nitrogen source is an ASTeX model AX4300 compact ECR source. The substrates, typically 1 in. in diameter or a quadrant of a 2-in. wafer, are mounted in a nonbonded holder. These substrates, after loading in the MBE system, are heat cleaned in a nitrogen plasma.

Growth of the GaN/AlGaN double heterostructure is initiated at the preferred GaN growth temperature, estimated to be 700 to 750°C, without the need for a low-temperature GaN buffer. The growth conditions, arrived at by a study [18] of the GaN material quality and growth rates as a function of the ECR source parameters, substrate temperature, and N_2 mass flow, are as follows: ECR forward power of 40–60 W, N_2 mass flow of 3.3 sccm, and substrate thermocouple temperature of 950°C. These conditions result in 300-K Hall electron mobilities of 200–270 cm^2/V s for GaN with 2×10^{17} cm^{-3} electron concentrations, grown on (0001) sapphire. These mobility values are typical for this growth method [19],[20], and the growth conditions are assumed to be optimal for the laser structures. GaN growth rates are as high as 0.18 μm/h. The first double heterostructure grown consisted of a top cladding layer of $Al_{0.1}Ga_{0.9}N$, 1000 Å thick, followed by the GaN active layer, 1000 Å thick, and a bottom cladding layer of $Al_{0.1}Ga_{0.9}N$, 5000 Å thick. In a second heterostructure, the active layer thickness was increased to 4000 Å.

Figure 2-2 shows a scanning electron micrograph (SEM) of the surface morphology of the double-heterostructure laser grown on the polished HVPE substrate. For comparison, Figure 2-3 shows the surface morphology of the double-heterostructure waveguide grown on (0001) sapphire using the two-step process with a 100-Å-thick low-temperature GaN buffer. While both surfaces are textured, the fine-grain morphology observed in layers grown directly on sapphire by ECR-MBE is absent in layers grown on the HVPE buffer. The remaining features of the material grown on the HVPE buffer may result from the polishing and cleaning processes prior to growth, and are not necessarily due to growth-induced defects. This is supported by the morphology obtained by growth on unpolished HVPE buffers, as shown in Figure 2-4, where the scalloped pattern of the polished GaN buffers is absent.

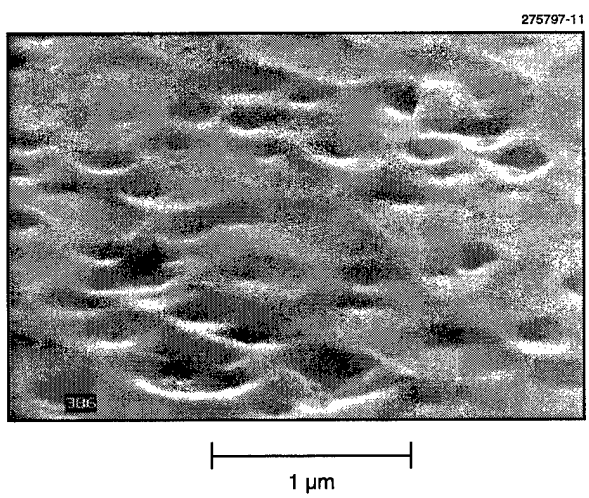

Figure 2-2. Scanning electron micrograph (SEM) of double-heterostructure surface morphology grown on polished hydride vapor phase epitaxy (HVPE) GaN buffer.

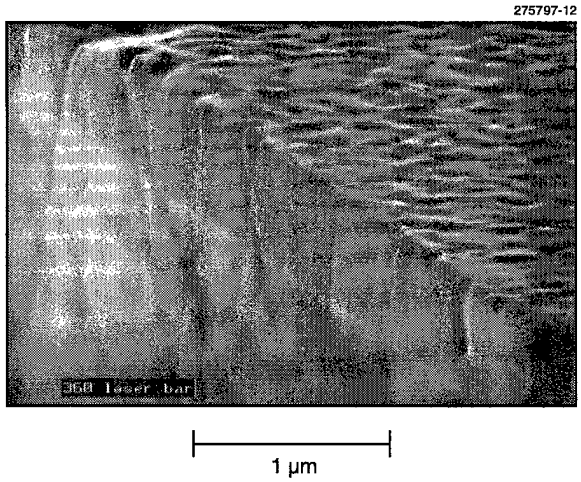

Figure 2-3. SEM of double-heterostructure surface morphology grown directly on (0001) sapphire.

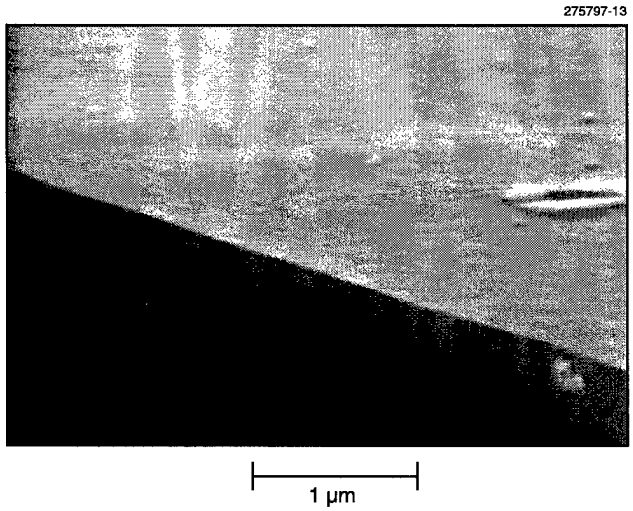

Figure 2-4. SEM of double-heterostructure surface morphology grown on unpolished (as-grown) HVPE GaN buffer.

Figure 2-5 shows the output energy as a function of pump fluence of a 65-μm-long cavity, at 77 and 300 K. Both curves show a threshold and a linear dependence above threshold, characteristic of stimulated emission. Based on the focused pump beam spot size of 2 × 0.2 mm, the calculated pump fluence is 0.3 mJ/cm^2 at 77 K, and 0.5 mJ/cm^2 at 300 K. The optical modes for this cavity length, however, could not be resolved. The 77-K emission spectrum from a shorter, saw-cut, 23-μm cavity is shown in Figure 2-6, where the cavity modes are clearly visible. The measured mode spacing of 0.56 nm corresponds to a group refractive index of 5.0, which is in agreement with the refractive index data of GaN [21].

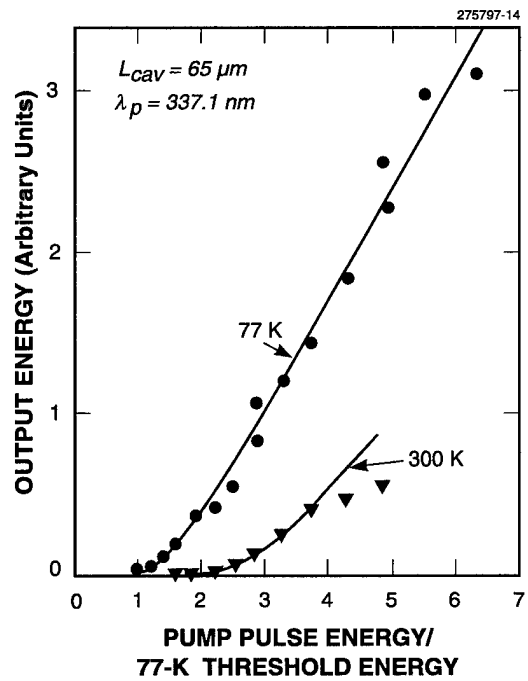

Figure 2-5. Transversely optically pumped edge emission output energy as a function of normalized pump pulse energy at 77 and 300 K for double heterostructure grown on polished HVPE GaN buffer. The cavity is 65 μm long, with saw-cut facets.

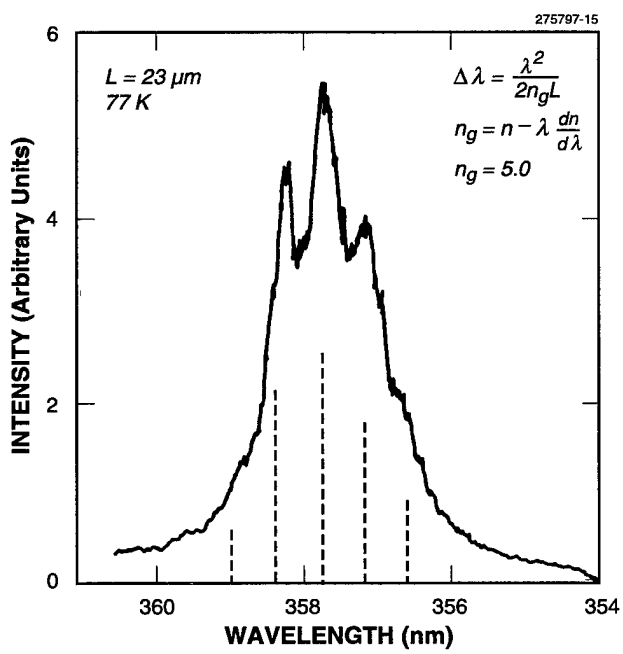

Figure 2-6. Emission spectrum at 77 K of cavity 23 μm long, with saw-cut facets. The vertical dashed lines indicate mode positions; the mode spacing is 0.56 nm.

Measurements of the far-field radiation pattern of the laser indicated a double-lobed intensity pattern in the plane perpendicular to the plane of the heterostructure, indicative of poor confinement of the optical field to the 1000-Å-thick GaN active layer. In order to improve the mode confinement, a second structure was grown with a 4000-Å-thick GaN active layer, this time on an unpolished HVPE buffer. The laser cavity was formed by breaking along the GaN cleavage planes of the thick buffer. The resulting intensity vs pump characteristic and the layer structure are shown in Figure 2-7 for a 1-mm-long cavity at 77 K. The emission spectrum near threshold and above threshold is shown in Figure 2-8. No attempt has yet been made to resolve mode structure with a short cavity for this heterostructure. The calculated threshold fluence is 0.15 mJ/cm^2 (threshold pump power of 0.25 MW/cm^2). The far-field pattern exhibits an angular width (full width at half-maximum) of 60°, which is consistent with the 4000-Å-thick active layer. Based on the far-field pattern, and measurements of the output energy of the laser, the estimated external quantum efficiency is 1%.

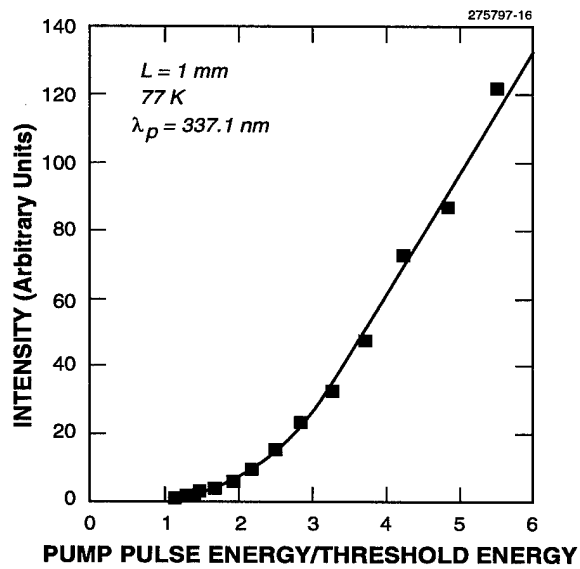

(a)

1000 Å AlGaN x = 0.1 CLADDING LAYER	
4000 Å GaN	ACTIVE LAYER
2000 Å AlGaN x = 0.1 CLADDING LAYER	
UNPOLISHED HVPE GaN BUFFER	

(b)

Figure 2-7. (a) Transversely pumped edge emission output energy as a function of normalized pump pulse energy at 77 K for double heterostructure grown on unpolished HVPE GaN buffer. The cavity is 1 mm long, with cleaved facets. (b) Laser structure.

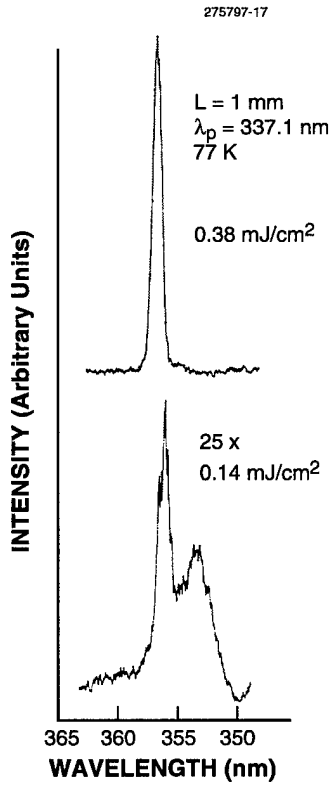

Figure 2-8. Emission spectrum at threshold (E_p = 0.14 mJ/cm^2) and above threshold (E_p = 0.38 mJ/cm^2) for double heterostructure, shown in Figure 2-7, grown on unpolished HVPE GaN buffer, with cleaved facets.

The use of HVPE buffers as substrates has enabled the convincing demonstration of laser action with mode structure for GaN/AlGaN double heterostructures grown by ECR-MBE. This establishes the feasibility of using HVPE GaN buffers, grown on sapphire, as substitutes for bulk GaN substrates. The results also indicate that ECR-MBE has potential as a technique for the development of GaN/AlGaN diode lasers.

P. A. Maki
R. J. Molnar
R. L. Aggarwal
Z. L. Liau
I. Melngailis

2.3 175-K CW OPERATION OF InAsSb/InAlAsSb/InAs QUANTUM-WELL DIODE LASERS EMITTING AT 3.5 μm

High-performance diode lasers emitting between 2 and 5 μm are very desirable for sensitive detection of trace gases because many molecules have fundamental absorption lines in this wavelength band. The sensitivity is typically higher by two orders of magnitude at the fundamental absorption lines than at overtones that appear in the near infrared.

At ~ 2 μm, antimonide-based strained quantum-well (QW) lasers, consisting of compressively strained GaInAsSb active layers and AlGaAsSb barrier/cladding layers, have exhibited excellent room-temperature performance [22]. However, the performance of diode lasers emitting beyond 3 μm has not been very good. The maximum CW operating temperature reported for III-V diode lasers is 128 K, which was obtained for InAsSb/InAlAsSb strained QW lasers grown on GaSb substrates with emission at ~ 3.9 μm [23].

Further improvement of such lasers has been found to be very difficult because of the presence of an extremely large miscibility gap for InAlAsSb on GaSb substrates [24]. However, the region of stable growth for InAlAsSb is somewhat larger on InAs. Here, we report much improved InAsSb/InAlAsSb QW lasers grown on InAs substrates. These lasers emitting between 3.2 and 3.55 μm have exhibited pulsed operation up to 225 K and CW up to 175 K, which to our knowledge are the highest temperatures for any III-V diode lasers in this wavelength range.

The following QW laser structure was grown on (100)-oriented n-type InAs substrates in a solid-source molecular beam epitaxy system with a valved As_2 cracking source: 0.5-μm-thick n^+-InAs buffer, 2-μm-thick n-$AlAs_{0.16}Sb_{0.84}$ cladding, QW active region consisting of ten 10-nm-thick $InAs_{0.935}Sb_{0.065}$ wells and eleven 20-nm-thick $In_{0.85}Al_{0.15}As_{0.9}Sb_{0.1}$ barriers, 2-μm-thick p-$AlAs_{0.16}Sb_{0.84}$ cladding, and 50-nm-thick p^+-GaSb cap layer. The wells are under compressive strain by ~ 0.45%, and the barriers are under tensile strain by 0.27% for strain balancing. Because the InAlAsSb alloy is close to the miscibility gap and the growth conditions were not optimized, the double-crystal x-ray diffraction pattern showed quite broadened satellite peaks, indicating that the interfacial quality is not very good.

Broad-stripe lasers 100 μm wide were fabricated by using SiO_2 patterning. For both n and p contacts, nonalloyed Ti/Pt/Au was used. Lasers were mounted junction-side up on Cu heat sinks using In, and loaded into a dewar for low-temperature measurements. The voltage vs current characteristic shows a high turn-on voltage, especially at low temperatures, because there are large barriers between the substrate and n cladding as well as between the n cladding and the active region. No graded layers were incorporated at these interfaces.

Figure 2-9 shows pulsed threshold current density J_{th} as a function of temperature for a 1000-μm-long device. At 80 K, the value of J_{th} is 60 A/cm^2. At this temperature, the contribution of Auger recombination to J_{th} may be small. A very high characteristic temperature T_0 (> 50 K) below 100 K may be attributed to slowly increasing interfacial recombination current resulting from nonoptimized interfaces. Between 100 and 200 K, T_0 is 30–40 K, which is typical for Auger-dominated devices. The maximum operating temperature is 225 K.

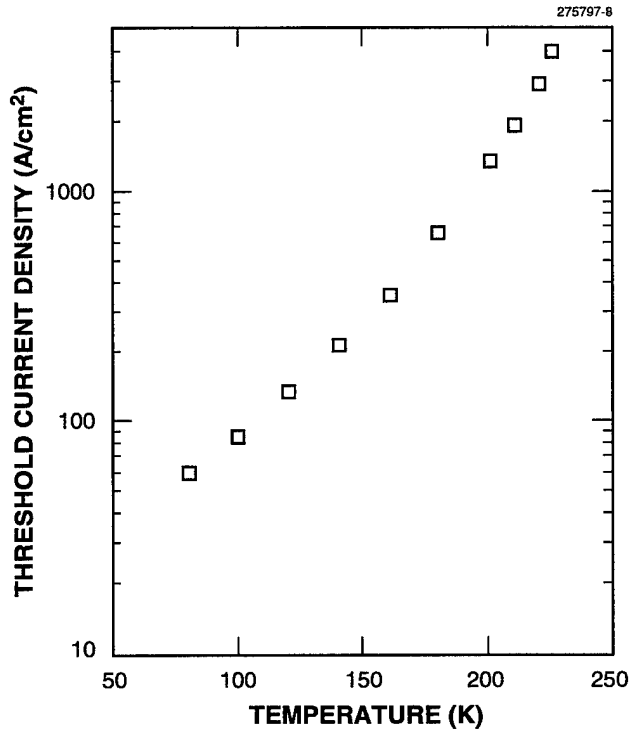

Figure 2-9. Pulsed threshold current density vs temperature of InAsSb/InAlAsSb quantum-well diode lasers.

Figure 2-10 shows the relative differential efficiency as a function of temperature. The efficiency remains more or less constant up to 140 K, and then decreases gradually. Even at 200 K, the efficiency remains at approximately one-third of the low-temperature values. In contrast, the efficiency of the double-heterostructure lasers decreases much more rapidly with temperature [25]. The emission wavelength at 80 K is 3.32 μm. The wavelength shifts to longer values at a rate of ~ 1 nm/K at low temperatures, but the rate gradually increases at higher temperatures and reaches ~ 2 nm/K at 220 K. The bandgap energy decreases more rapidly at higher temperatures.

Figure 2-11 shows the CW power vs current curves for an 8-μm-wide ridge-waveguide laser at several temperatures. At 100 K, the CW threshold current is 12 mA. The differential quantum efficiency is ~ 30% from both facets, which is slightly smaller than ~ 35% obtained for the broad-stripe lasers. Although it is not shown in Figure 2-11, the maximum CW power at 100 K is more than 10 mW/facet. The maximum CW operating temperature is 175 K, where the threshold current is 102 mA. In general, the emission spectrum shows multilongitudinal modes. The emission wavelength at 175 K is 3.48 μm. The lateral far-field pattern shows a single lobe with a full width at half-maximum of 24°.

H. K. Choi
G. W. Turner
M. J. Manfra
M. K. Connors
D. R. Calawa
J. W. Chludzinski
W. L. McGilvary

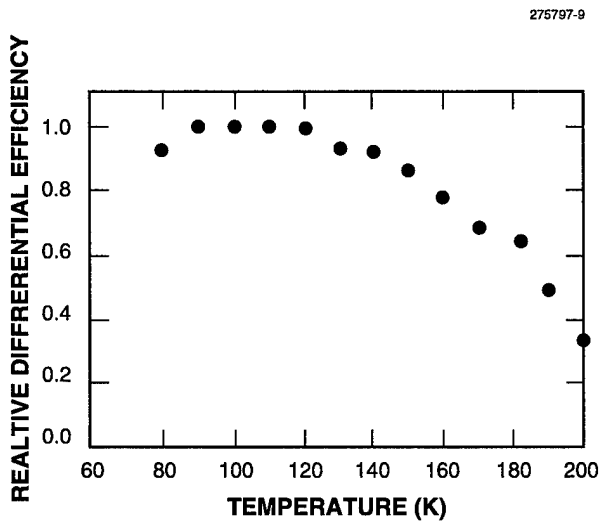

Figure 2-10. Dependence of relative differential efficiency on temperature.

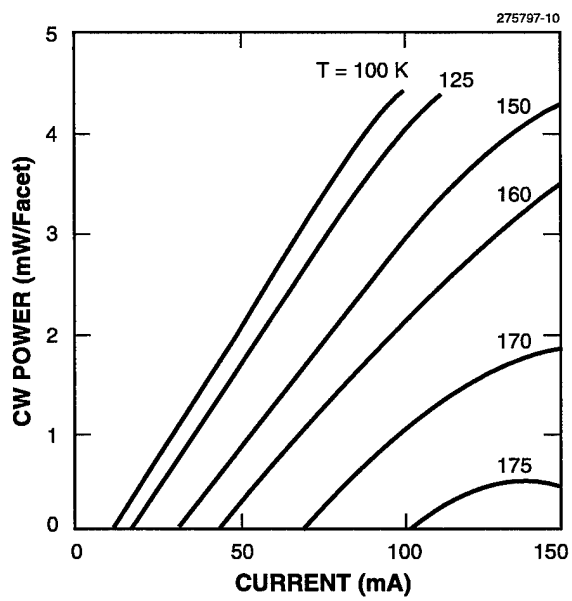

Figure 2-11. CW power vs current of ridge-waveguide laser at several temperatures. The width and length of the laser are 8 and 1000 μm, respectively.

REFERENCES

1. See, for example, I. Akasaki and H. Amano, *J. Electrochem. Soc.* **141**, 2266 (1994).
2. See, for example, S. Nakamura, M. Senoh, N. Iwasa, and S. Nagahama, *Appl. Phys. Lett.* **67**, 1868 (1995).
3. S. D. Lester, F. A. Ponce, M. G. Craford, and D. A. Steigerwald, *Appl. Phys. Lett.* **66**, 1249 (1995).
4. W. Qian, M. Skowronski, M. De Graef, K. Doverspike, L. B. Rowland, and D. K. Gaskill, *Appl. Phys. Lett.* **66**, 1252 (1995).
5. See, for example, M. Born and E. Wolf, *Principles of Optics*, 6th ed. (Pergamon, Oxford, 1980), p. 463.
6. R. L. Aggarwal, P. A. Maki, R. J. Molnar, Z. L. Liau, and I. Melngailis, *J. Appl. Phys.* **79**, 2148 (1996).
7. P. A. Maki, R. J. Molnar, R. L. Aggarwal, Z. L. Liau, and I. Melngailis, to be published in *Mater. Res. Soc. Symp. Proc.*
8. R. J. Molnar, R. L. Aggarwal, Z. L. Liau, E. R. Brown, I. Melngailis, W. Götz, L. I. Ramano, and N. M. Johnson, to be published in *Mater. Res. Soc. Symp. Proc.*
9. S. Nakamura, T. Mukai, and M. Senoh, *Appl. Phys. Lett.* **64**, 1678 (1994).
10. X. H. Yang, T. J. Schmidt, W. Shan, J. J. Song, and B. Goldenbert, *Appl. Phys. Lett.* **66**, 1 (1995).
11. A. S. Zubrilov, V. I. Nikolaev, D. V. Tsvetkov, V. A. Dmitriev, K. G. Irvine, J. A. Edmond, and C. H. Carter, Jr., *Appl. Phys. Lett.* **67**, 533 (1995).
12. H. Amano, T. Asahi, and I. Akasaki, *Jpn. J. Appl. Phys.* **29**, 205 (1990).
13. I. Akasaki, H. Amano, N. Koide, M. Kotaki, and K. Manabe, *Physica B* **185**, 428 (1993).
14. H. Amano, N. Watanabe, N. Koide, and I. Akasaki, *Jpn. J. Appl. Phys.* **32**, 1000 (1993).
15. M. A. Khan, S. Krishnankutty, R. A. Skogman, J. N. Kuznia, D. T. Olson, and T. George, *Appl. Phys. Lett.* **65**, 520 (1994).
16. K. Yung, J. Yee, J. Koo, M. Rubin, N. Newman, and J. Ross, *Appl. Phys. Lett.* **64**, 1135 (1994).
17. R. J. Molnar, K. B. Nichols, P. Maki, E. R. Brown, and I. Melngailis, *Mater. Res. Soc. Symp. Proc.* **378**, 479 (1995).
18. Solid State Research Report, Lincoln Laboratory, MIT, 1995:1, p. 21.
19. M. E. Lin, B. Sverdlov, G. L. Zhou, and H. Morkoç, *Appl. Phys. Lett.* **62**, 3479 (1993).
20. R. J. Molnar, R. Singh, and T. D. Moustakas, *J. Electron. Mater.* **24**, 275 (1995).
21. E. Ejder, *Phys. Status Solidi* **6**, 445 (1971).

22. H. K. Choi, G. W. Turner, and S. J. Eglash, *IEEE Photon. Technol. Lett.* **6**, 7 (1994).

23. H. K. Choi and G. W. Turner, *Appl. Phys. Lett.* **67**, 332 (1995).

24. K. Onabe, *NEC Res. Dev.* **72**, 1 (1984).

25. H. Q. Le, G. W. Turner, S. J. Eglash, H. K. Choi, and D. A. Coppeta, *Appl. Phys. Lett.* **64**, 152 (1994).

3. SUBMICROMETER TECHNOLOGY

3.1 HIGH-RESOLUTION STUDIES OF CRYSTALLINE DAMAGE INDUCED BY SINGLE-POINT DIAMOND MACHINING OF SILICON

Recent advances in machining silicon using single-point diamond lathes have identified a regime where material removal is ductile, rather than brittle, and the resultant material has been observed to have less damage as determined by surface roughness [1]. This has great importance for fabrication of optical components. We have focused on the nature and extent of the much more subtle damage and subsurface phenomena, such as localized defects in the atomic arrangement of single crystals, since these phenomena have not yet been investigated.

A standard commercially available single-point diamond machining (SPDM) tool was used to machine the Si(100) surfaces in this study. No special preparations were made with the diamond tool bit, which had a radius R of 64 μm and a rake angle of -25°. Two passes were made by the diamond tool over the silicon surfaces. The first pass was a semi-finish-quality machining step and used a rotation rate N of 800 rpm, an in-feed rate f of 1.27 mm/min (1.59 μm/rev), and a depth of cut of 25.4 μm. The final pass used values of N = 800 rpm and f = 0.76 mm/min (0.95 μm/rev). The four depths of cut evaluated were 1.27, 12.7, 25.4, and 50.8 μm and were obtained as four 12-mm-wide annuli on a single 100-mm-diam Si(100) wafer, with the shallowest depth of cut starting at the outside of the wafer. This corresponds to average silicon removal rates of 4.5×10^6, 3.2×10^7, 3.8×10^7, and 2.6×10^7 $\mu m^3/s$, respectively, and the tool velocity was 4.2 m/s at the outside of the wafer and 0.17 m/s near the center where the machining was stopped. This change in tool velocity was not expected to be of major consequence, as previous reports [1],[2] have indicated the tool speed to have little effect on the critical depth for the brittle-to-ductile transition. In addition, three coolant fluids were evaluated for their chemical interactions during the removal process: water, odorless mineral spirits, and mineral oil.

The resultant silicon surfaces showed significant variations in macroscopic roughness depending upon the machining direction, with the <100> exhibiting significantly more damage than the <100>. This result is in agreement with previous experiments of SPDM of Si(100) [3]. Figure 3-1 summarizes the surface roughness data as obtained by both atomic force microscopy (AFM) and optical interferometry for the <100> direction; the <100> direction was too rough for measurement using these techniques. Figures 3-2(a) and 3-2(b) show representative scanning electron microscopy and AFM images, respectively, of the <100> direction for a 25.4-μm depth of cut.

The high-resolution transmission electron microscopy (HRTEM) results of the same samples show several types of crystalline damage extending below the surface. The first type of damage observed is dislocation loops and the second is slip planes along a specific direction, 53.7° from the {100} plane, indicating that the slip planes preferentially propagate along the {111} planes. The maximum observed depth for each type of damage is plotted vs depth of cut both for the <100> and <100> directions in Figures 3-3(a) and 3-3(b), respectively.

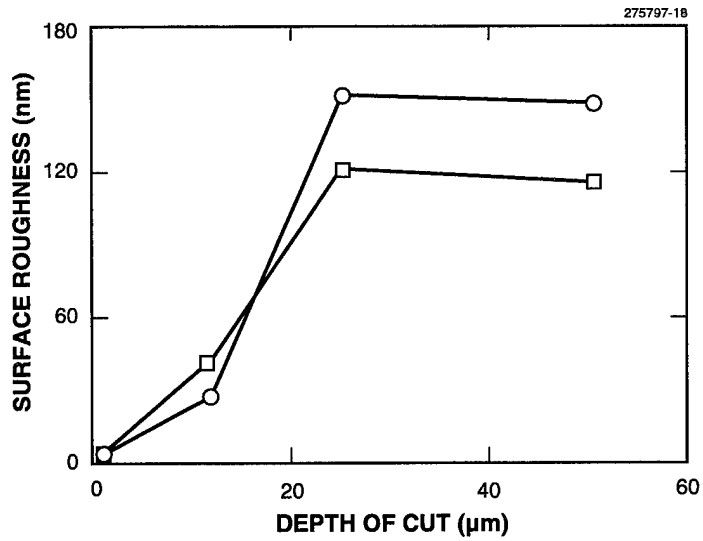

Figure 3-1. Root-mean-square surface roughness for Si(100) that has been single-point diamond machined (SPDM) as a function of depth of cut. The tool radius was 64 μm, the feed rate was 0.95 μm/rev, and the lubricating/cooling fluid was odorless mineral spirits. The data shown compare rms roughness measured by atomic force microscopy (circles) to that obtained by optical interferometry (squares). For the above data, the diamond point was traveling parallel to the <100> direction.

In addition to the HRTEM analysis, x-ray photoemission spectroscopy (XPS) was performed on samples machined using lubricants which were both carbon based (odorless mineral spirits and mineral oil) and non–carbon based (water). All samples were degreased with organic solvents prior to analysis. In either case, no evidence was found for the formation of anything other than standard carbon contamination and common silicon passivation, as indicated by the carbon 1*s* and silicon 2*p* spectra. No evidence for SiC formation was found. In addition, angle-resolved XPS measurements revealed relatively thick layers (2–5 nm) of carbon (CH_x) contamination on samples machined using carbon-based lubricants.

Previous reports on SPDM of silicon have focused both on characterizing a brittle-to-ductile yield transformation [1],[2],[4],[5] and on crystallographic orientation effects [3]. No previous analysis of the nature or extent of the *subsurface* damage as a function of tool-sample interaction was performed, either for ductile or brittle yield regimes. For both <100> and <110> orientations we see subsurface crystalline damage extending to a maximum depth of roughly 3 μm. Although slip planes propagate to depths greater than ~ 0.8 μm for all the instances examined by us, it is notable that the surface roughness *can* be reduced to near theoretical limits. In fact, when the depth of cut was reduced to 1.27 μm, surface roughness of 4–5 nm rms was observed. This value agrees well with roughness of 3–4 nm obtained in a previous study under ideal conditions, and is close to the limiting roughness under our experimental conditions ($f = 0.95$ μm/rev and $R = 64$ μm) of ~ 2 nm as derived from the following equation in [1]:

$$\text{Minimum roughness} = f^2/8R \ . \tag{3.1}$$

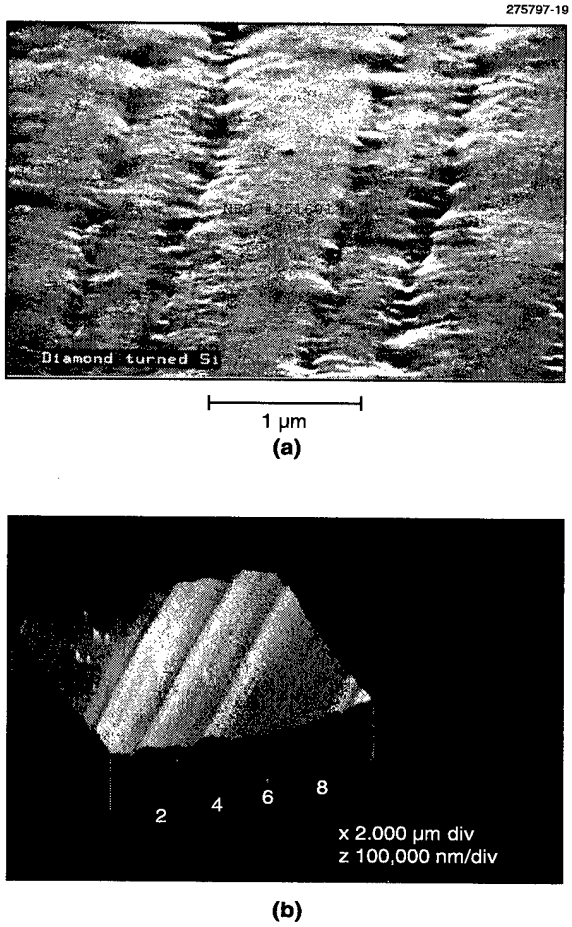

Figure 3-2. (a) SEM of Si(100) that resulted from SPDM parallel to the <100> direction. The depth of cut was 25.4 µm, the tool radius was 64 µm, and the feed rate was 0.95 µm/rev. Two machining passes were made with ~ 50 µm of material removed. (b) Atomic force microscopy image of Si(100) from SPDM parallel to the <100> direction. The conditions and amount of material removed are similar to those for the sample shown in (a).

The roughness values obtained for Si(100) are generally higher than those obtained for Ge(100) [1]. One reason that has been postulated [1] is increased tool wear in the case of silicon, as a result of tip-surface interactions and/or chemical reactions. High-temperature reactions resulting in SiC formation could potentially lead to such effects. However, our observations that show no SiC formation do not support this theory.

The brittle-to-ductile transition can be described by the relative energies required for plastic deformation (ductile yield) and fracturing (brittle yield). For ductile yield, the required energy E_{ductile} is

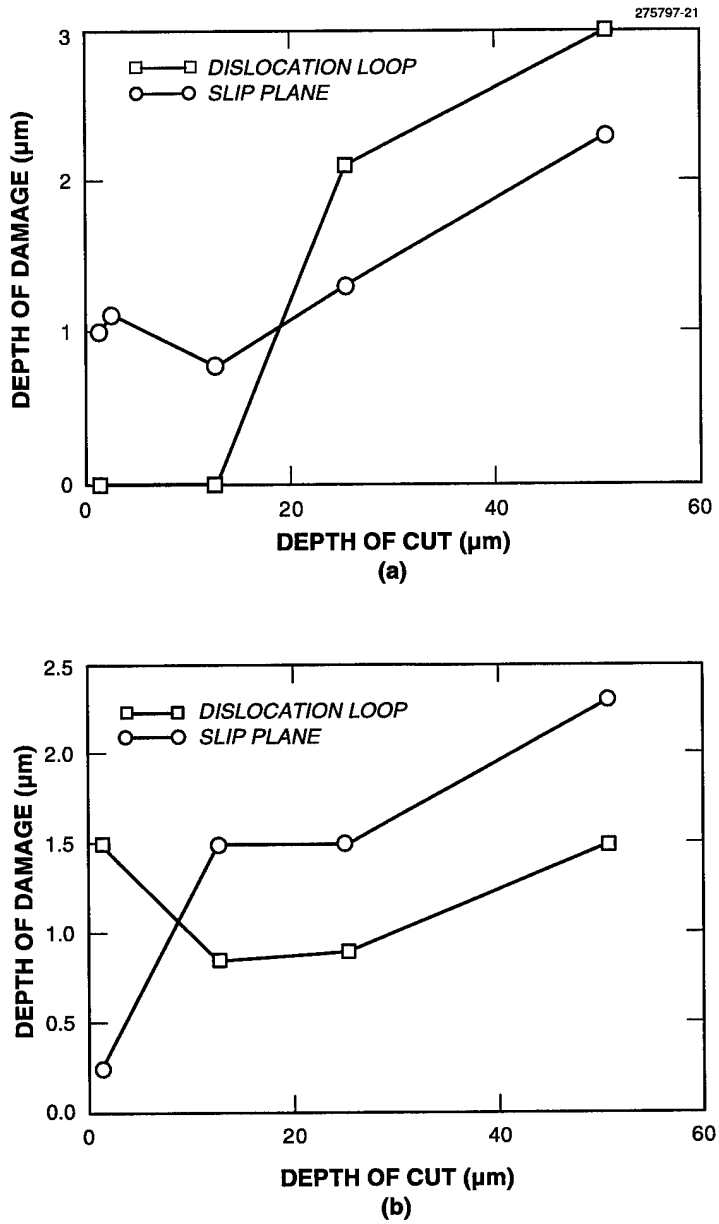

Figure 3-3. Depth of crystalline damage as observed by transmission electron microscopy as a function of depth of cut for Si(100) from SPDM parallel to the (a) <100> and (b) <110> directions. The two curves show the damage depth for dislocation loops (squares) and slip planes along the {111} plane (circles).

governed not only by the yield stress σ_y for that material, but also by the volume of material being deformed, i.e.,

$$E_{\text{ductile}} = A\,\sigma_y d^3 \ , \tag{3.2}$$

where d is the chip size removed along the cut shoulder and is governed by the feed rate f. The brittle fracture energy E_{brittle} is governed by the Griffith crack propagation parameter G and the area of the new surface a crack will create, i.e.,

$$E_{\text{brittle}} = BGd^2 \ . \tag{3.3}$$

In Equations (3.2) and (3.3), A and B are constants of proportionality. Ductile yield becomes favored over brittle yield when $E_{\text{ductile}} < E_{\text{brittle}}$. This condition is satisfied for small values of d when $d < (B/A)(G/\sigma_y)$. In this regime, yield mechanisms other than crack formation will be present [2]. Under our experimental conditions, for single-pass SPDM the cut shoulder will be in the brittle regime. However, for multipass machining the brittle damaged zone along the cut shoulder is often removed in subsequent passes, leaving behind only plastically deformed material even when $d > (B/A)(G/\sigma_y)$.

Interpretation of the nature and origin of the subsurface damage can be better understood by using Figure 3-4 [4]. Shoulder-cut analysis [1],[4],[5] of SPDM Si(100) indicates a transition below which the yielded chip size is too large for plastic yield. This transition occurs when the machined depth is at some critical depth d_c at distance z from the tool center, as seen in Figure 3-4. At cut depths greater than d_c, microfractures result from the brittle yield and extend to a characteristic depth y_c. Ductile material removal is obtained when the microfracture zone y_c does not extend below the cut surface plane, i.e., when $y_c < a$, as in Figure 3-4. We have estimated the value of a for our experiments by using

$$\sin\theta = d_c / f \ , \tag{3.4}$$

$$\sin(\theta/2) = b/2R \ , \tag{3.5}$$

$$d_c = [f(z+f)]/R \ , \tag{3.6}$$

and

$$a^2 + z^2 = b^2 \ , \tag{3.7}$$

where Equations (3.4) and (3.6) are from [4] and a and b are from Figure 3-4. Combining these equations, setting $\sin\theta = \theta$ (for small θ), and rearranging yield

$$a = \left[(2Rd_c/f) - f^2\right]^{1/2} \ , \tag{3.8}$$

which is the upper limit on fracture depth before the resultant surface cracks are not machined away in subsequent tool passes (i.e., when $y_c < a$). Since $f^2 << 2Rd_c/f$, we can present a simplified expression for a (for our conditions of R = 64 μm and f = 0.95 μm/rev)

$$a \sim 11.6 d_c^{1/2} \ . \tag{3.9}$$

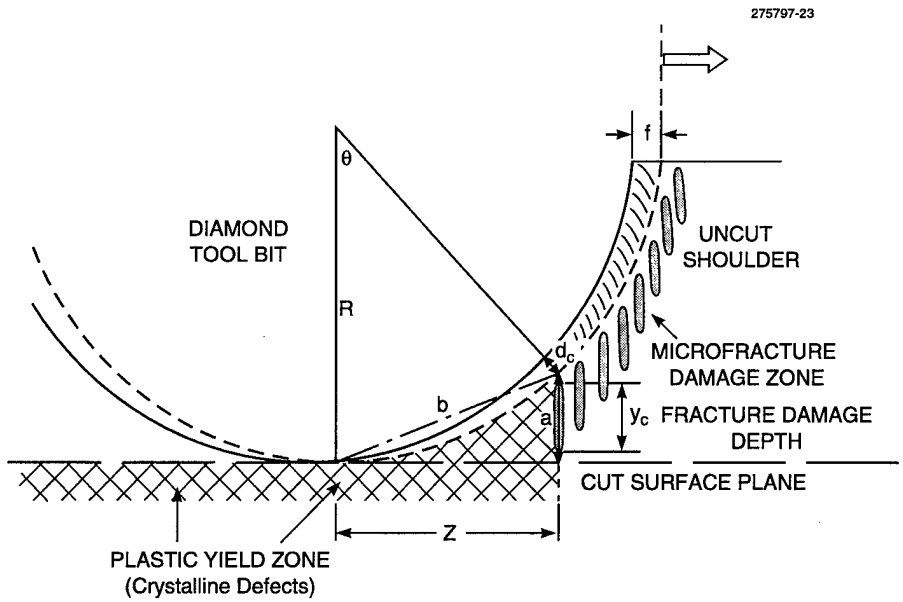

Figure 3-4. Schematic diagram of geometry for SPDM (reproduced in part from Ref. 4). In the diagram, f is the feed rate (m/rev), y_c is the brittle fracture damage (crack) depth, d_c is the critical depth for the brittle-to-ductile transformation, R is the tool radius, and a, b, and z are geometric parameters used to define the conditions when the brittle fracture crack depth propagates below the cut surface plane.

Previous experimental measurements [4] on Si(100) have led to estimates for d_c of 0.1 to 0.2 μm using SPDM with a tool radius (76 μm) and rake angle (–10° to –30°) similar to those used in this study. Other estimates [5] for d_c of 0.1 μm for "favorable" crystallographic orientations, such as the <100>, have also been reported. These values for d_c suggest that a is in the range 3.6–5.2 μm, as compared to values of y_c of 0.5–1 μm derived from shoulder-cut experiments [4]. This result suggests that the fracture damage depth is less than a for our experiments and the resulting subsurface damage zones observed by HRTEM are ductile yield zones. Thus, the crystalline damage is a characteristic of plastic deformation.

Interestingly, the Equations (3.4)–(3.9) do not show any dependence of a on the depth of cut. However, the data in Table 3-1 show a transition from ductile to brittle material removal upon going to deeper depths of cut. From this, we assume that y_c may depend on factors relating to the tool-surface geometry along the cut shoulder, such as a relationship between brittle fracture depth and the removed chip size. As the depth of cut is reduced, perhaps the amount of brittle material removal along the cut shoulder decreases, thereby decreasing y_c. When y_c becomes less than a, this may signify the transition to ductile removal.

R. R. Kunz
H. R. Clark
P. M. Nitishin
M. Rothschild
B. S. Ahern

TABLE 3-1

Root-Mean-Square Surface Roughness of Si(100) Single-Point Diamond Machined along the <100> Direction*

Depth of Cut (μm)	rms Roughness	
	Atomic Force Microscopy (nm)	Wyko (nm)
1.27	4.4	5.1
12.7	28	42
25.4	151	121
50.4	149	116

*Conditions are as outlined in the text.

REFERENCES

1. P. N. Blake and R. O. Scattergood, *J. Am. Ceram. Soc.* **73**, 949 (1990).
2. T. Bifano, T. Dow, and R. O. Scattergood, *Proc. SPIE* **966**, 108 (1988).
3. W. S. Blackley and R. O. Scattergood, *J. Am. Ceram. Soc.* **73**, 3113 (1990).
4. W. S. Blackley and R. O. Scattergood, *Precision Eng.* **13**, 95 (1991).
5. C. K. Syn, J. S. Taylor, R. R. Donaldson, and S. Shimada, presented at the 1988 Spring Meeting of the Japanese Society of Precision Engineering, Kawasaki, Japan, March 1988.

4. HIGH SPEED ELECTRONICS

4.1 CORRELATION OF OPTICAL PULSES WITH A LOW-TEMPERATURE-GROWN GaAs PHOTOCONDUCTOR

A novel sampling correlator is described that is useful for characterizing optical pulses with subpicosecond temporal resolution. The correlator exploits the ultrafast nonlinear response of a photoconductor made of low-temperature-grown (LTG) gallium arsenide, which is connected to a coplanar-waveguide transmission line. Unlike commercially available correlators, the LTG-GaAs correlator (LTGGC) does not require a nonlinear crystal for second-harmonic generation. Instead, the LTGGC uses a nonlinearity that is associated with the transmission line and photoconductor functioning as a voltage divider. The resulting nonlinearity is used to measure $g^{(2)}(\tau)$, the second-order intensity autocorrelation function [1].

Figure 4-1 schematically shows the LTG-GaAs photoconductor in a transmission line geometry. On time scales of ~ 1 ps, the current response $i_{pc}(t)$ to an intensity pulse $I(t)$ is effectively instantaneous.

$$i_{pc}(t) = \frac{V_o}{Z_o + G(t)^{-1}} \quad . \tag{4.1}$$

Here, V_o is the dc bias voltage, Z_o is the characteristic impedance of the transmission line (~ 100 Ω), and $G(t) \propto I(t)$ is the photoconductance [2]. For small $I(t)$, the photocurrent $i_{pc}(t)$ is linear in $I(t)$ since $G(t)^{-1} >> Z_o$ and the photoconductor is voltage biased. For larger $I(t)$, however, the photoconductor is no longer voltage biased—it is biased through a load impedance Z_o and responds nonlinearly in $I(t)$ when $Z_o \approx G^{-1}$.

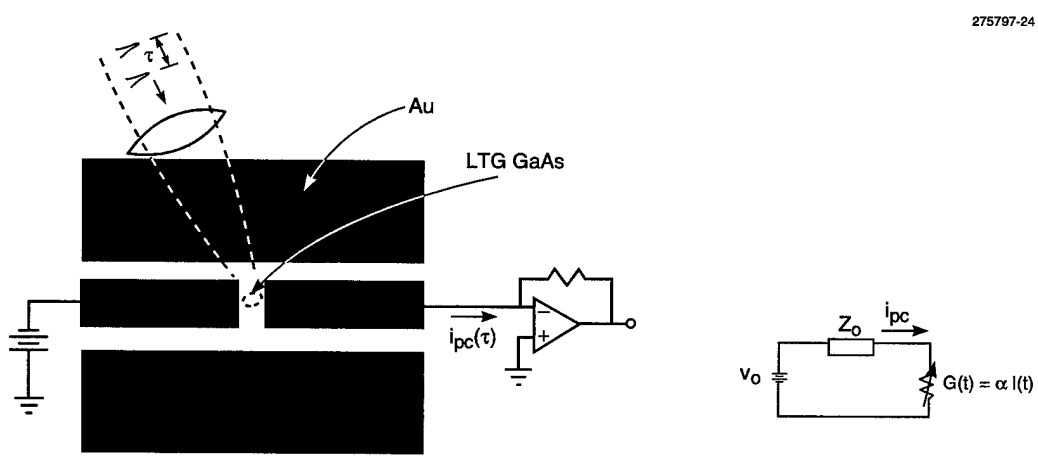

Figure 4-1. Schematic diagram of low-temperature-grown (LTG) GaAs photoconductor embedded in coplanar-waveguide transmission line. A transimpedance amplifier is used as a readout for the dc photocurrent $i_{pc}(t)$. The equivalent circuit models the high-frequency response of the LTG GaAs correlator (LTGGC) to an intensity pulse $I(t)$.

This nonlinearity is exploited by the LTGGC to measure $g^{(2)}(\tau)$ as follows. Phenomenologically, the lowest-order nonlinearity is given by $i_{pc}(t) \approx S_I^{(2)} (I(t))^2$, where $S_I^{(2)}$ is the second-order nonlinear current responsivity in units of A/(W cm^{-2})^2. For two cross-polarized beams that are separated by a variable time delay τ, the incident intensity at the LTG-GaAs photoconductor is $I_T(t) = I(t) + I(t + \tau)$. The time-averaged photocurrent in response to $I_T(t)$ gives a cross-term which depends on τ:

$$< i_{pc}(\tau) >_t = 2S_I^{(2)} < I(t)I(t+\tau) >_t + \text{const} \quad . \tag{4.2}$$

Neglecting the constant term, $< i_{pc}(\tau) >_t$ is proportional to the second-order intensity autocorrelation $g^{(2)}(\tau)$ in the limit that the photoconductor nonlinear responsivity $S_I^{(2)}$ depends weakly on $I(t)$—a condition that is satisfied when the intensity is chosen such that $Z_oG \approx 0.1$. Therefore, $g^{(2)}(\tau)$ can be measured from the dc photocurrent as a function of the time delay τ.

An example illustrates typical parameter values for the LTGGC. Consider a photoconductor integrated into a coplanar waveguide, as shown in Figure 4-1, with a 5 × 5-μm active area. Assume the quantum efficiency $\eta = 0.5$, $\hbar\omega = 1.5$ eV, photoconductive response time $\tau_r = 100$ fs, electron mobility $\mu_e = 100$ cm^{2}V/s, and hole mobility $\mu_h << \mu_e$. For a 100-Ω transmission line, the optimum operating condition $Z_oG \approx 0.1$ occurs for a peak intensity $I(t) = 7 \cdot 10^7$W/cm^2. This corresponds to an average power of 0.1 mW for a mode-locked Ti:sapphire laser that produces ~ 80-fs pulses at a repetition rate of 82 MHz. This power is much lower than that required for a similar signal-to-noise ratio for conventional autocorrelators (typically ~ 10 mW) [3].

The temporal resolution of the LTGGC is determined by the time required for the LTG-GaAs photoconductor to return to a high resistance state after brief illumination. This recovery time is referred to as τ_r—which accounts for recombination and trapping of photoexcited electrons and holes. Time-domain reflectivity measurements were used to measure τ_r in a LTG-GaAs sample. In such measurements, a short intense pulse induces a change in the reflectivity ΔR, which then decays exponentially with time constant τ_r. The lifetime τ_r measured for our sample was ~ 650 fs.

We recently demonstrated the feasibility of the LTGGC using this photoconductor sample. The temporal resolution of this particular LTGGC is limited by τ_r and is adequate for measuring intensity envelopes with modulation features on time scales longer than ~ 1 ps. A 10 × 3-μm LTG-GaAs photoconductor was integrated into a high-frequency coplanar waveguide patterned from a Au:Ti metal film. An audio speaker with a retroreflector driven at 30 Hz swept the time delay τ between two trains of ~ 80-fs pulses from a Ti:sapphire laser. The two pulse trains were coupled to the LTG-GaAs photoconductor through a length of single-mode optical fiber. The optical fiber dispersed the ~ 80-fs pulses to picosecond time scales. Figure 4-2(a) shows a measurement of $i_{pc}(\tau)$ vs time delay τ for two ~ 80-fs optical pulse trains ($\lambda = 810$ nm) that have propagated through 43 cm of single-mode optical fiber. The shape of this curve is similar to autocorrelation curves measured for dispersed pulses with a conventional autocorrelator [4]. The sharp peak in the center is a coherence peak whose width is approximately

the inverse of the pulse's optical bandwidth. The coherence peak contains no information about the time scale of the modulated intensity and can be eliminated by coupling the two optical pulses with crossed polarizations through a polarization-maintaining optical fiber. The rounded shoulders on either side of the coherence peak contain information about the temporal width of the dispersion-broadened pulse. The full width at half-maximum of the rounded shoulders is 2 ps for Figure 4-2(a). Deconvolution, assuming a $\text{sech}^2(t)$ pulse shape, then yields a temporal width of 1.3 ps for the dispersed optical pulse. Figure 4-2(b) shows a similar measurement but with a longer length of fiber (94 cm). Deconvolution in this case yields a width of 1.9 ps for the dispersed pulse. The curves in Figure 4-2 clearly demonstrate the operation of the LTGGC on the picosecond time scale. Note that the coherence peak has the same width in both traces. This indicates that the bandwidth has been preserved and that the LTGGC is not measuring a change in coherence—it is measuring the additional dispersion of the intensity envelope caused by the longer optical fiber.

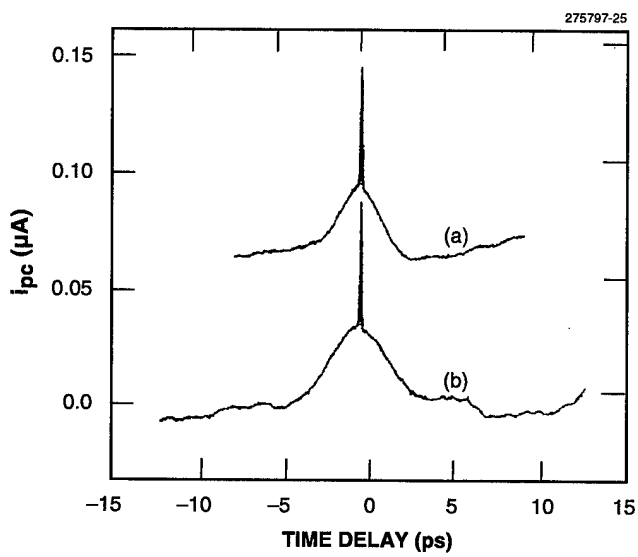

Figure 4-2. Demonstration of LTGGC used to measure dispersion on the 1-ps time scale. (a) Measured values of $i_{pc}(\tau)$ vs time delay τ for two optical pulses that have been dispersed by propagating through 43 cm of single-mode optical fiber. (b) Measured values of $i_{pc}(\tau)$ vs τ for two optical pulses that have propagated through 94 cm of fiber. The LTGGC clearly measures the increased dispersion produced by the longer fiber.

Compared to conventional autocorrelators that use nonlinear crystals, the LTGGC allows for simplified and compact measurement of the intensity-intensity autocorrelation function of picosecond optical pulses. Faster LTG-GaAs photoconductors are being developed with τ_r approaching 100 fs [5]. Such a photoconductor would conceivably make the LTGGC useful for characterizing optical pulses produced by femtosecond lasers.

S. Verghese
N. Zamdmer*
E. R. Brown
A. Forster*
Q. Hu*

REFERENCES

1. E. P. Ippen and C. V. Chank, in *Ultrashort Light Pulses*, S. L. Shapiro, ed. (Springer-Verlag, New York, 1977), pp. 83-122.
2. E. R. Brown, K. A. McIntosh, F. W. Smith, M. J. Manfra, and C. L. Dennis, *Appl. Phys. Lett.* **62**, 1206 (1993).
3. For example, the Model 5-14 autocorrelator, Inrad Corp., Northvale, N.J.
4. K. L. Sala, G. A. Kenney-Wallace, and G. E. Hall, *IEEE J. Quantum Electron.* **QE-16**, 990 (1980).
5. K. A. McIntosh, private communication.

*Author not at Lincoln Laboratory.

5. MICROELECTRONICS

5.1 USE OF A CHARGE-COUPLED DEVICE AS A CHARGED-PARTICLE SPECTROMETER

Charge-coupled devices (CCDs) are well known as detectors of electromagnetic radiation and can additionally provide spectroscopic information for photons in the soft-x-ray portion of the spectrum. CCDs can also readily detect energetic charged particles and have been used in the field of nuclear physics to determine particle tracks. In principle, the CCD can also provide spectroscopic information on charged particles, although there appears to have been relatively little work on this use of the device. We describe here measurements of the energy of alpha particles from 1.8 to 5.5 MeV using a large-area CCD imager. These results can be extrapolated to show that CCDs can be a valuable diagnostic tool in analyzing energetic particles emerging from an inertial confinement fusion implosion.

The device used in these measurements was a front-illuminated 1024×1024-pixel imager with four output ports [1]. This device was made on material comprising a 10–12-μm epitaxial layer of 40-Ω cm resistivity grown on a 0.01-Ω cm p^+ substrate. For the higher energies, where the particle penetrates through the device epilayer into the p^+ substrate, the length of the particle track in the active portion of the device (and therefore the collected charge) depends on the angle of incidence of the particle. To minimize this effect, we placed the particle source as far as possible from the device and limited the analyzed data to a 256×512 portion of the imaging area from one port where the particles were incident at no more than 10° from normal. The device temperature was –20°C, and we clocked it at a frame rate of ~ 0.5 Hz. As a source of charged particles we used 0.5 μCi of Am^{241}, which emits essentially monoenergetic alpha particles at 5.49 MeV. The energy of the particles was varied by inserting various thicknesses of polyimide and mylar films between the source and the CCD to degrade the energy of the particles. At each energy we typically collected 50–100 frames, each with about 20 α events, in order to produce a suitable spectrogram.

Figure 5-1 is a plot of pixel amplitudes from an 18×18-pixel portion of one frame showing two events from unattenuated particles. A 5.5-MeV α particle will penetrate to a depth of 25 μm in the device (after taking into account the energy losses in the device surface layers), and therefore the ionization trail extends through the entire epilayer. In this case about 800 000 electrons from each trail are collected in the CCD wells. The charge generated in the deeper portion of the device undergoes substantial lateral diffusion, so that the collected event charge spreads across 2–3 pixels. In addition, the charge in the central well of each event usually exceeds the well capacity (about 130 000 e^-), and therefore some spreading, or "blooming," of the charge into adjacent pixels along the direction of charge transfer also occurs. Typically, the event charge for this energy will occupy from 7 to 12 pixels, depending on the location of the α-particle track with respect to the pixel boundaries. Because the desired spectroscopic information resides in the total charge generated, it is critical that the blooming not occur under conditions of charge pumping. This means either that the CCD clocks must not operate in inversion, or that blooming must occur without trapping of the electrons at surface states if the device is to be operated with inverted surfaces. In our case we chose to keep the low rail of the clocks just above the inversion point so that no charge pumping losses occurred.

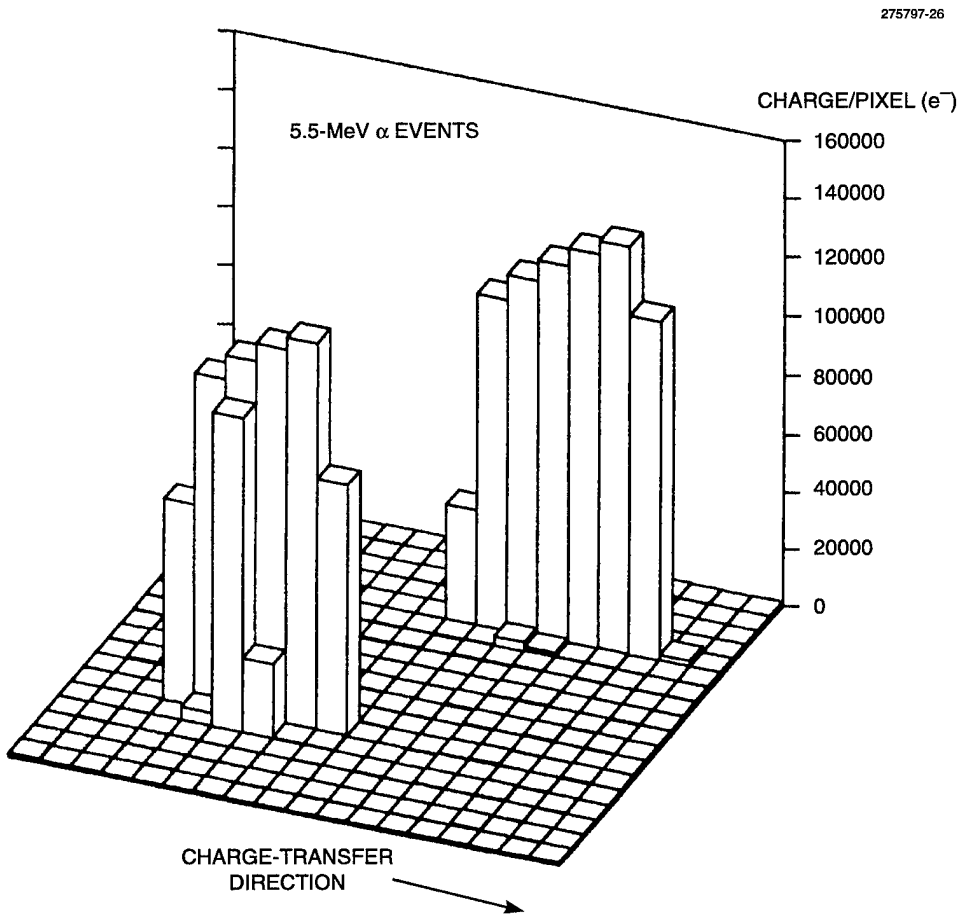

Figure 5-1. Plot of pixel signal amplitudes for small region of front-illuminated charge-coupled device (CCD) containing three events from α particles of 5.5 MeV incident on the device. The charge created by each particle covers several pixels and totals about 800 000 e^-.

Figure 5-2 shows the results of the measured and calculated CCD response as a function of α-particle energy. The energy E_m measured by the CCD was obtained from the average total electron count $\overline{N}$ for the events, using the formula $E_m = \overline{N} \cdot E_{pair}$, where $E_{pair} = 3.65$ eV is the energy required to generate an electron-hole pair in silicon. The calculated curve is based on the range and energy loss data from the computer program TRIM [2], and includes the loss of particle energy in the surface layers (1 μm of scratch-protection SiO_2 and 0.8 μm of gate insulator and polysilicon). This energy deposition contributes no signal charge, but it manifests itself as an intercept of ~ 0.5 MeV when extrapolating the CCD data to zero charge. For energies up to ~ 4 MeV the particle has a range less than the epilayer thickness, and therefore essentially all the charge in the ionization trail is collected by the CCD wells. At higher energies the particle has a range extending into the p^+ substrate, but it is clear from the data that only a portion of the charge deposited in the p^+ material is being collected. The effective collection depth appears to be ~ 16 μm, or roughly 3–6 μm into the p^+ substrate, and from this we can estimate a minority carrier lifetime on the order of 100 ns. This is in good agreement with the estimated Auger lifetime of 50–100 ns for 0.01-Ω cm p-type silicon [3].

The spectroscopic capability of a CCD for charged particles can be used to great benefit as a diagnostic in inertial confinement fusion research. A conceptual design of a spectrometer comprising an array of CCDs in combination with a magnet to provide some momentum separation of the particles can in principle yield the identity and energy of charged particles from a fusion implosion [4]. The particles of interest in this application are protons, deuterons, and tritons, and their energies range from ~ 1 to nearly 31 MeV. The energy losses per unit distance, however, are substantially lower for such particles

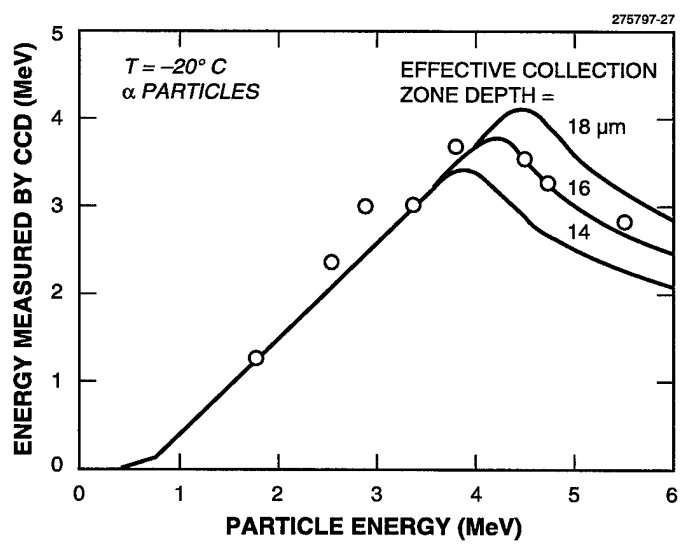

Figure 5-2. Measurements of energy deposited in CCD for α particles from Am^{241} whose energy has been degraded by varying thicknesses of polyimide films.

than those of alpha particles, and the estimated charge deposited in 10 μm of silicon ranges from ~ 10 000 to 300 000 e^-. These values are within the achievable well capacities yet comfortably above the read noise of current CCDs. This means that the event charge should occupy fewer pixels, and this allows for a higher particle flux to be measured. Although the large signals allow some margin for additional dark current noise and therefore alleviate the need for cooling the device, the displacement damage resulting from particle bombardment will ultimately raise the dark current and may dictate a modest amount of cooling. The relatively large charge levels in this application make the issue of charge-trapping losses from displacement damage a much less serious issue than in situations such as x-ray spectroscopy or low-light-level imaging. Thus, the CCD is in many respects very well suited to this type of diagnostic.

B. E. Burke R. D. Petrasso*
T. Hotaling C. K. Li*

REFERENCES

1. Solid State Research Report, Lincoln Laboratory, MIT, 1993:4, p. 39.
2. J. F. Ziegler, J. P. Biersack, and U. Littmark, *The Stopping and Range of Ions in Solids* (Pergamon, New York, 1985).
3. S. M. Sze, *Physics of Semiconductor Devices* (John Wiley, New York, 1981), p. 144.
4. D. G. Hicks, C. K. Li, R. D. Petrasso, K. W. Wenzel, and J. P. Knauer, MIT Plasma Fusion Center Report RR-94-11, November 1994.

*Author not at Lincoln Laboratory.

6. ANALOG DEVICE TECHNOLOGY

6.1 MICROWAVE POWER DEPENDENCE OF $YBa_2Cu_3O_7$ THIN-FILM JOSEPHSON EDGE JUNCTIONS

The power dependence of the microwave-frequency surface impedance of the high-T_c superconductors continues to be of interest, both to advance fundamental materials understanding and to enhance the power-handling capability of high-performance superconducting microwave filters. While the power dependence has not been fully understood, it has been suggested that material defects acting as weak links with Josephson-junction behavior are the source of the nonlinearities [1]. This work reports the first measurements of the power dependence of Josephson junctions fabricated in high-T_c superconductors. The results are explained through the use of the resistively shunted Josephson-junction (RSJ) model.

The use of stripline resonators to measure the nonlinearity of the surface impedance has been described [2]. In the test structure for the measurements presented here, the Josephson junction is located precisely at the midpoint of the stripline resonator, extending across the full 150-μm width. The Josephson junction is a superconductor/normal-metal/superconductor edge junction of composition $YBa_2Cu_3O_7$/ $YBa_2CoCu_2O_7$/$YBa_2Cu_3O_7$ (YBCO/YBCoCO/YBCO), and has been described in detail elsewhere [3]. Since the rf current of the odd resonant modes has a peak at the midpoint of the stripline, the junction exerts maximum influence on these modes. The even resonant modes are unaffected by the presence of the junction.

Figure 6-1 shows typical results for the effective resistance of the junctions, R, vs the microwave current I_{rf}. The results are derived from measurements at T = 70 K of the resonator Q vs input power for the fundamental mode n = 1, f_0 = 1.8 GHz and the first overtone mode n = 2, f_0 = 3.6 GHz. The measurements show that at low powers R of mode 1 is smaller than that of mode 2 in approximately the ratio 1:4 as would be expected for a surface resistance R_S proportional to f_0^2. As I_{rf} is increased, however, R of mode 1 increases sharply and crosses that of mode 2. As will be discussed below, the more rapid increase of R of mode 1 occurs when the I_{rf} exceeds the critical current of the Josephson junction. The shape of the R vs I_{rf} curve for mode 2 is similar to that of YBCO films we have reported previously [1]. Figure 6-2 shows R vs I_{rf} for mode 1 for several temperatures from 11 to 70 K, demonstrating the same general behavior. The solid lines are fits to the data by a model discussed in detail below.

The data were analyzed by the application of the RSJ model [4] to the situation of the rf current flowing in the resonator. We solve the RSJ equations

$$\frac{L_0}{R_n}\frac{d\phi}{dt} + \sin\phi = \frac{I}{I_C} \tag{6.1}$$

$$I_j = I_C \sin\phi \ , \tag{6.2}$$

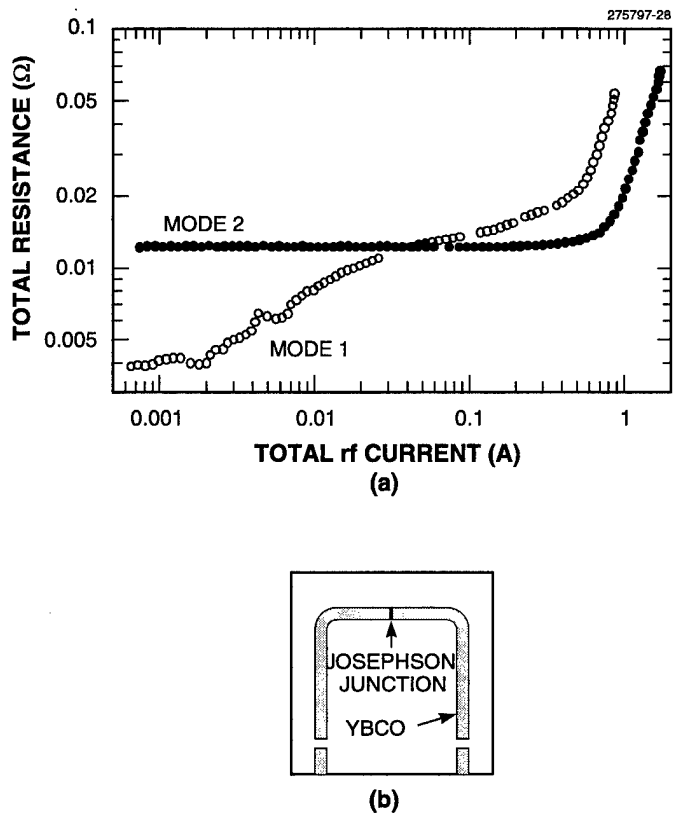

Figure 6-1. R vs I_{rf} for first two resonant modes of resonator at temperature T = 70 K. The open circles are for mode 1, f_0 = 1.8 GHz. The solid circles are for mode 2, f_0 = 3.6 GHz. The inset shows a schematic view of the patterned center conductor of the resonator with Josephson junction. Not shown are the two ground planes above and below the strip.

where $L_0 = \Phi_0/2pI_C$ and $\Phi_0 = h/2e$ is the flux quantum, R_n is the normal resistance of the junction, ϕ is the phase difference across the junction, I is the total (time-dependent) current flowing in the shunted network, I_C is the critical current of the junction, and I_j is the Josephson current in the junction. The junction resistance as a function of the microwave current is obtained from the solution and averaged over the current distribution of the stripline. This procedure was used to calculate curves to compare with the experimental results. The measured resistance is the sum of the junction resistance and rf resistance of the remainder of the stripline, $R(I) = R_j(I) + R_{rf}(I)$. The constant R at low current shown in Figure 6-2 arises from the R_S of the film constituting the stripline because the calculated R_j is much smaller at very low currents. The I_C and R_n used in the calculation were varied separately to obtain a good visual fit to the data in the intermediate range of currents shown in Figure 6-2. The I_C values influence the point where R begins to increase, and R_n determines the limiting value of the calculated R at large I_{rf}. Table 6-1 shows the parameters used to obtain the fits to the data. As seen, the fits are very good in the low and intermediate ranges of I_{rf}, but at the highest values the measured R departs greatly from that calculated by the RSJ model.

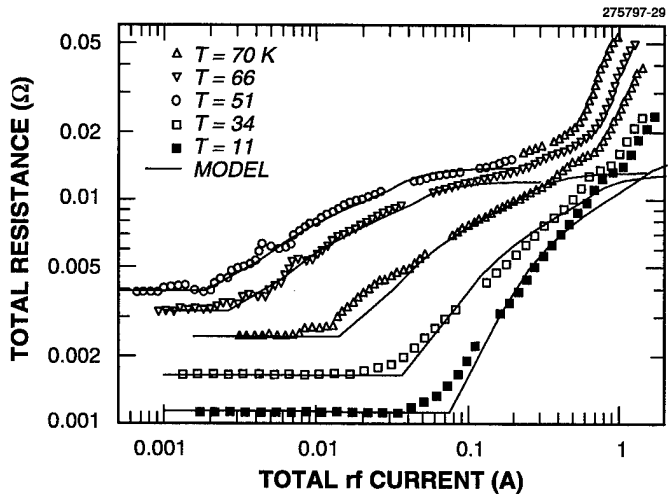

Figure 6-2. R vs I_{rf} for mode 1 at various temperatures as indicated in the figure. The solid lines are fits to the data by the resistively shunted Josephson-junction model. The parameters of the fits for each temperature are given in Table 6-1.

TABLE 6-1

Values of I_c and R_n Used to Obtain Fits to Data

Temperature (K)	I_c (A)	R_n (Ω)
70	0.021	0.01
66	0.029	0.009
51	0.156	0.011
34	0.4	0.011
11	0.8	0.015

The initial rise in R occurs when the current density $J(x)$ exceeds the critical current density of the junction at the edge of the stripline, which in Figure 6-2 occurs at the value of I_{rf} that is about 10% of the total critical current because of the high $J(x)$ at the edge of the stripline. The flat part of the curve after the initial rise indicates the asymptotic approach to R_n at large currents, which is predicted by the RSJ model. The sharp rise at high currents happens when the current is 10–100 times larger than at the initial rise and cannot be understood from the RSJ model calculation. A possible explanation of the effect is hysteretic loss [5] due to flux entry into the junction that leads to a substantial change in the current distribution. Effects similar to the behavior of mode 2 in Figure 6-1 at high current are seen in measurements on striplines without junctions [1]. However, the behavior of mode 1 is due to the junction because R is higher than that of mode 2. This departure from the RSJ model needs further investigation. One enhancement to the model would be inclusion of a distribution of junctions with differing parameters.

Figure 6-3 shows the temperature dependence of the critical current density J_C obtained from the fits compared with that obtained from dc current-voltage measurements on films of similar quality and thickness [3]. The J_C was obtained by dividing the I_C by the cross-sectional area of the film, 150 μm × 0.2 μm in the case of the stripline used here, and 18 μm × 0.2 μm for the dc measurements. As seen in Figure 6-3, the agreement between the rf and dc determination of J_C is excellent.

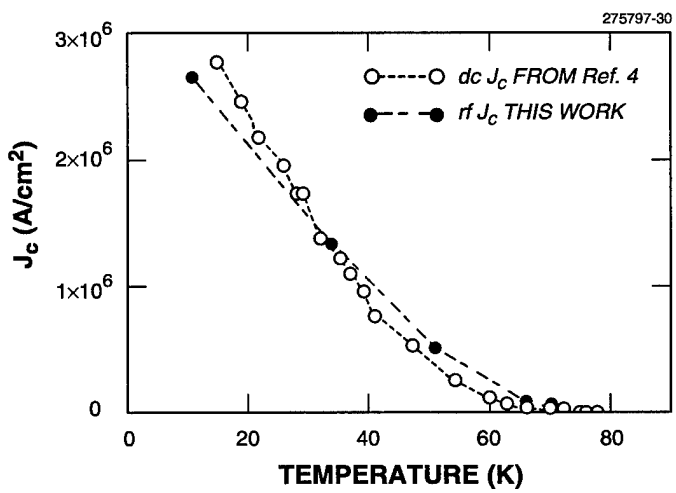

Figure 6-3. J_c as determined in this work from fits to the rf resistance (closed circles) compared to that determined from dc current-voltage measurements on films of similar quality as reported in Ref. 4 (open circles).

These results are consistent with the idea that the power dependence of the films results from Josephson junctions included in the material. Further enhancement of the film model should lead to improved theoretical understanding.

D. E. Oates
P. P. Nguyen*
Y. Habib*
G. Dresselhaus*
M. S. Dresselhaus*
G. Koren*
E. Polturak

REFERENCES

1. P. P. Nguyen, D. E. Oates, G. Dresselhaus, and M. S. Dresselhaus, *Phys. Rev. B* **48**, 6400 (1993).
2. D. E. Oates, P. P. Nguyen, G. Dresselhaus, M. S. Dresselhaus, C. W. Lam, and S. M. Ali, *J. Superconduct.* **5**, 361 (1992).
3. G. Koren, E. Polturak, D. Cohen, E. Aharoni, and L. Patlagan, *Physica C* **221**, 157 (1994).
4. T. VanDuzer and C. W. Turner, *Principles of Superconductive Devices and Circuits* (Elsevier, New York, 1981).
5. P. P. Nguyen, D. E. Oates, G. Dresselhaus, M. S. Dresselhaus, and A. C. Anderson, *Phys. Rev. B* **51**, 6686 (1995).

*Author not at Lincoln Laboratory.

7. ADVANCED SILICON TECHNOLOGY

7.1 LASER-PROGRAMMABLE GATE ARRAY

Gate arrays that allow programming of a complex logic function on a single chip in a matter of minutes have become a critical part of the electronic systems industry. They allow rapid integration of custom logic for interfacing standard components such as microprocessors, and increasingly they are able to incorporate some processor functions. Most of these circuits, the field-programmable gate arrays, are customized electronically by the user. An alternative, the laser-programmable gate array (LPGA), is inherently faster because its connections have low resistance (order of 1 Ω), and denser because no programming circuitry is required on the chip. One such LPGA is commercially available now, utilizing only laser cuts. That restriction precludes testing of chips before programming and requires tens of millions of laser operations. The ability to make low-resistance laser connections allows pretesting, and reduces the number of laser operations by 2 orders of magnitude.

Lincoln Laboratory and one of our DoD sponsors have developed such a laser connection and an LPGA that uses it. The present-generation chip, the LPGA-20k, can implement up to 20 000 gates, and an earlier version has been clocked at rates as high as 80 MHz. It is fabricated with 0.8-μm minimum dimensions and two metal layers in a manufacturing facility operated for the DoD by a major semiconductor manufacturer. This facility will soon convert to a 0.5-μm process with three metal layers, which should enable even larger and faster LPGAs. The novel laser connection has also been licensed to a startup company which will design and build its own LPGA.

The programmable connection requires no special fabrication steps. It comprises two parallel lines of standard aluminum alloy meeting the normal design rules of the fabrication process. Typically one line is a through-conductor and the other is a short tab of metal with a via connecting it to another through-conductor on a different metal layer, as illustrated in Figure 7-1. Before programming, nothing distinguishes this structure from any other wiring on the chip. The link is programmed by heating the two parallel lines with a laser pulse until the metal melts. Thermal expansion cracks the glass that surrounds the two metal lines and the crack is filled with liquid metal, which then freezes to form a permanent connection with $< 1\ \Omega$ resistance. A small number of experiments have indicated that these devices are reliable: in electromigration tests the metal line approaching the link fails before the link itself.

Many thousands of these links have been made successfully with three different lasers: 2-μs green light pulses from an argon ion laser, 10-ns pulses of about the same wavelength from a doubled Nd:YLF laser, and 10-ns infrared pulses (1047 nm) from the Nd:YLF without doubling. All of these work, but the Q-switched Nd:YLF in the infrared is preferred, with a pulse energy of ~ 1 μJ and spot diameter of ~ 6 μm. Doubling allows a smaller focused spot, but a small spot is not required for these links, and doubling degrades the pulse energy repeatability. The long pulse of the electrooptically shuttered argon laser does more damage than the short Q-switched pulse. In particular, the links illustrated in Figure 7-1 are designed to be redundant. There are two short tabs of metal on either side of the through-conductor, both connected to the same conductor on the other level, forming two link sites in parallel. With the 10-ns pulse, both of those sites can be linked, thereby providing redundancy along with reduced

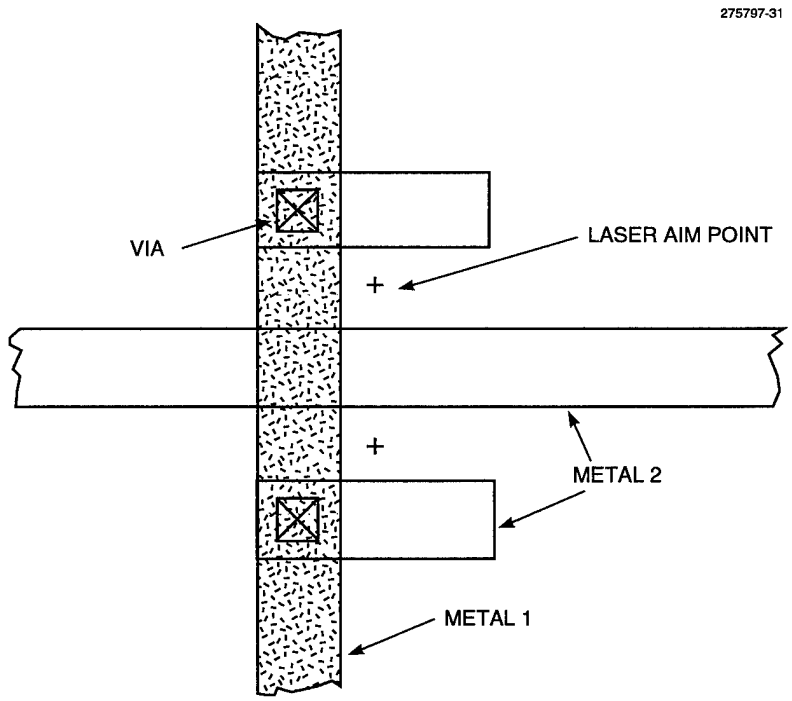

Figure 7-1. Typical redundant link layout. Metal 2 can be connected to metal 1 by a laser pulse at either or both of the indicated aim points.

resistance. With the longer pulse it was found that if one site is linked successfully and then a link is attempted at the second site, the connection is often broken. The long pulse, having much greater total energy, both breaks the original link and fails to form the second connection.

The LPGA-20k uses laser cutting as well as linking, and for cutting the advantage of the *Q*-switched laser is even greater. The argon laser gave failure rates on the order of one unmade cut per thousand attempts for aluminum-based lines with a window etched in the passivation glass at each cut site. With the *Q*-switched infrared laser many thousands of cuts have been made without failure as long as the pulse energy is correct. The range of acceptable pulse energy is presently being determined; it appears to be rather wide. As for linking, the energy is ~ 1 μJ, but for cutting the beam is focused to the minimum diameter of ~ 2.5 μm. Figure 7-2 shows a typical site after cutting. It is evident that the metal melts and separates during the laser pulse.

Cuts can also be made without any window in the passivation glass, but the overlying glass is severely damaged in the process. It is believed that the windows allow placing cutting sites closer to other structures, and hence allow higher density. For architectures that require only a few cuts, windows are not necessary, so passivation of unused sites can be maintained.

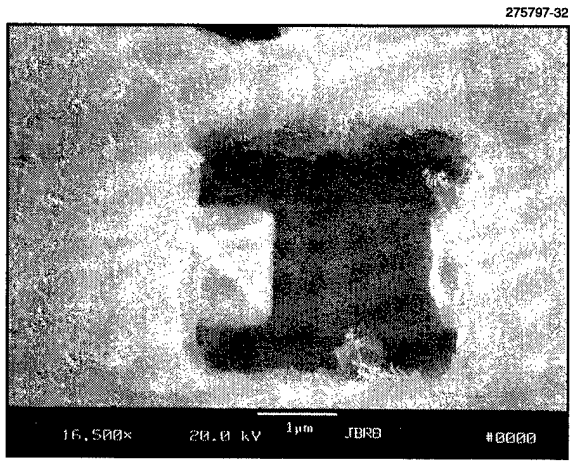

Figure 7-2. Scanning electron micrograph of a typical cut site after cutting. The metal was melted by a focused laser pulse near the center of the passivation window.

In future work, linking and cutting failure rates will be determined for larger numbers of operations, exceeding one million, and windows of acceptable pulse energy and spot size will be determined. The near-term goal is to enable both the DoD sponsor and the startup company to produce much larger gate arrays than the present LPGA-20k.

M. Fritze
R. S. Frankel
P. W. Wyatt

REPORT DOCUMENTATION PAGE

Form Approved
OMB No. 0704-0188

Public reporting burden for this collection of information is estimated to average 1 hour per response, including the time for reviewing instructions, searching existing data sources, gathering and maintaining the data needed, and completing and reviewing the collection of information. Send comments regarding this burden estimate or any other aspect of this collection of information, including suggestions for reducing this burden, to Washington Headquarters Services, Directorate for Information Operations and Reports, 1215 Jefferson Davis Highway, Suite 1204, Arlington, VA 22202-4302, and to the Office of Management and Budget, Paperwork Reduction Project (0704-0188), Washington, DC 20503.

1. AGENCY USE ONLY (*Leave blank*)	2. REPORT DATE	3. REPORT TYPE AND DATES COVERED
	15 February 1996	Quarterly Technical Report, 1 November 1995–31 January 1996

4. TITLE AND SUBTITLE

Solid State Research

5. FUNDING NUMBERS

C — F19628-95-C-0002
PE — 63250F
PR — 221

6. AUTHOR(S)

David C. Shaver

7. PERFORMING ORGANIZATION NAME(S) AND ADDRESS(ES)

Lincoln Laboratory, MIT
244 Wood Street
Lexington, MA 02173-9108

8. PERFORMING ORGANIZATION REPORT NUMBER

1996:1

9. SPONSORING/MONITORING AGENCY NAME(S) AND ADDRESS(ES)

HQ Air Force Materiel Command
AFMC/STSC
Wright-Patterson AFB, OH 45433-5001

10. SPONSORING/MONITORING AGENCY REPORT NUMBER

ESC-TR-96-060

11. SUPPLEMENTARY NOTES

None

12a. DISTRIBUTION/AVAILABILITY STATEMENT

Approved for public release; distribution is unlimited.

12b. DISTRIBUTION CODE

13. ABSTRACT (*Maximum 200 words*)

This report covers in detail the research work of the Solid State Division at Lincoln Laboratory for the period 1 November 1995–31 January 1996. The topics covered are Electrooptical Devices, Quantum Electronics, Materials Research, Submicrometer Technology, High Speed Electronics, Microelectronics, and Analog Device Technology. Funding is provided primarily by the Air Force, with additional support provided by the Army, ARPA, Navy, BMDO, NASA, and NIST.

14. SUBJECT TERMS

quantum electronics, electrooptical devices, materials research, submicrometer technology, high-speed electronics, microelectronics, analog device technology, advanced silicon technology, Josephson edge junctions, single-point diamond machining, photoconductors, charge-coupled devices, lasers, gate arrays

15. NUMBER OF PAGES 78

16. PRICE CODE

17. SECURITY CLASSIFICATION OF REPORT	18. SECURITY CLASSIFICATION OF THIS PAGE	19. SECURITY CLASSIFICATION OF ABSTRACT	20. LIMITATION OF ABSTRACT
Unclassified	Same as Report	Same as Report	Same as Report